
Inverse Problems and Parameter Identification in Image Processing

Michail Kulesh¹, Benjamin Berkels², Kristian Bredies³, Christoph Garbe⁴,
Jens F. Acker⁵, Mamadou S. Diallo⁶, Marc Droske², Matthias
Holschneider¹, Jaroslav Hron⁵, Claudia Kondermann⁴, Peter Maass³,
Nadine Olischläger², Heinz-Otto Peitgen⁷, Tobias Preusser⁷, Martin
Rumpf², Frank Scherbaum⁸, and Stefan Turek⁵

¹ Institute for Mathematics, University of Potsdam,
Am Neuen Palais 10, 14469 Potsdam, Germany
{mkulesh,hols}@math.uni-potsdam.de

² Institute for Numerical Simulation, University of Bonn,
Wegelerstr. 6, 53115 Bonn, Germany
{benjamin.berkels,nadine.olischlaeger,martin.rumpf}@ins.uni-bonn.de

³ Center of Industrial Mathematics (ZeTeM), University of Bremen,
Postfach 33 04 40, 28334 Bremen, Germany
{kbredies,pmaass}@math.uni-bremen.de

⁴ Interdisciplinary Center for Scientific Computing, University of Heidelberg,
Im Neuenheimer Feld 368, 69120 Heidelberg, Germany
{Christoph.Garbe,Claudia.Nieuwenhuis}@iwr.uni-heidelberg.de

⁵ Institute for Applied Mathematics, University of Dortmund, Vogelpothsweg 87,
44227 Dortmund, Germany
{jens.acker,jaroslav.hron,ture}@math.uni-dortmund.de

⁶ Now at ExxonMobil Upstream Research company, Houston, Texas, USA
mamadou.s.diallo@exxonmobil.com

⁷ Center for Complex Systems and Visualization, University of Bremen,
Universitätsallee 29, 28359 Bremen, Germany
{heinz-otto.peitgen,preusser}@cevis.uni-bremen.de

⁸ Institute for Geosciences, University of Potsdam, Karl-Liebnecht-Strasse 24,
14476 Potsdam, Germany fs@geo.uni-potsdam.de

1.1 Introduction

Many problems in imaging are actually inverse problems. One reason for this is that conditions and parameters of the physical processes underlying the actual image acquisition are usually not known. Examples for this are the inhomogeneities of the magnet field in magnetic resonance images leading to nonlinear deformations of the anatomic structures in the recorded images, material parameters in geological structures as unknown parameters for the simulation of seismic wave propagation with sparse measurement on the sur-

face, or temporal changes in movie sequences given by intensity changes or moving image edges and resulting from deformation, growth and transport processes with unknown fluxes. The underlying physics is mathematically described in terms of variational problem or evolution processes. Hence, solutions of the forward problem are naturally described by partial differential equations. These forward models are reflected by the corresponding inverse problems as well. Beyond these concrete, direct modeling links to continuum mechanics abstract concepts from physical modeling are successfully picked up to solve general perceptual problems in imaging. Examples are visually intuitive methods to blend between images showing multiscale structures at different resolution or methods for the analysis of flow fields.

This chapter is organized as follows. In Sect. 1.2 wavelet based method for the identification of parameters describing heterogeneous media in subsurface structures from sparse seismic measurements on the surface are investigated by Kulesh, Holschneider, Scherbaum and Diallo. It is shown how recent wavelet methodology gives further insight and outperforms classical Fourier techniques for these applications.

In Sect. 1.3 close links between surface matching and morphological image matching are established. Berkels, Droske, Olischläger and Rumpf describe how to encode image morphology in terms of the map of regular level set normals (the Gauss map of an image) and the singular normal field on edges. Variational methods are presented to match these geometric quantities of images in a joint Mumford Shah type approach. These techniques are complemented by a related approach for explicit surface matching in geometric modeling.

In Sect. 1.4 anisotropic diffusion models with a control parameter on the right hand side are investigated by Bredies, Maass and Peitgen. The aim is a visually natural blending between image representations on different scales. The method is applied for the morphing between medical images of different detail granularity. Here the transition between different scales is captured by the diffusion, whereas the right hand side of the corresponding parabolic initial value problem is considered as a control parameter to ensure that the coarse scale image is actually meet at time 1 starting from the fine scale image at time 0. Existence of solution for this type of control problem is established.

The inverse problem of optical flow is investigated in Sect. 1.5. Here, the focus is in particular on restoration methods for dense optical flow and the underlying image sequence. Garbe, Kondermann, Preusser and Rumpf describe confidence measure for local flow estimation and flow inpainting based on variational techniques. Furthermore, Mumford Shah type approaches for joint motion estimation and image segmentation as well as motion deblurring are presented. Finally, Acker, Hron, Preusser and Rumpf consider in Sect. 1.6 multiscale visualization methods for fluid flow based on anisotropic diffusion methods from image processing. Here, efficient finite element methodology is investigated to resolve temporal flow patterns in a perceptually intuitive way

based on time dependent texture mapping. In addition algebraic multigrid methods are applied for a hierarchical clustering of flow pattern.

1.2 Inverse Problems and Parameter Identification in Geophysical Signal Processing

Surface wave propagation in heterogeneous media can provide a valuable source of information about the subsurface structure and its elastic properties. For example, surface waves can be used to obtain subsurface rigidity through inversion of the shear wave velocity. The processing of experimental seismic data sets related to the surface waves is computationally expensive and requires sophisticated techniques in order to infer the physical properties and structure of the subsurface from the bulk of available information.

Most of the previous studies related to these problems are based on Fourier analysis. However, the frequency-dependent measurements, or time-frequency analysis (TFR) offer additional insight and performance in any applications where Fourier techniques have been used. This analysis consists of examining the variation of the frequency content of a signal with time and is particularly suitable in geophysical applications.

The continuous wavelet transform (CWT) of a real or complex signal $S(t) \in L^2(\mathbb{R})$ with respect to a real or complex mother wavelet is the set of L^2 -scalar products of all dilated and translated wavelets with this signal Holschneider [1995]:

$$\begin{aligned} \mathcal{W}_g S(t, a) &= \langle T_t D_a g, S \rangle = \int_{-\infty}^{+\infty} \frac{1}{a} g^* \left(\frac{\tau - t}{a} \right) S(\tau) d\tau, \\ S(t) &= \mathcal{M}_h \mathcal{W}_g S(t, a) = \frac{1}{C_{g,h}} \int_{-\infty}^{+\infty} \int_{-\infty}^{+\infty} h \left(\frac{t - \tau}{a} \right) \mathcal{W}_g S(\tau, a) \frac{d\tau da}{a^2}, \end{aligned} \quad (1.1)$$

where g, h are wavelets used for the direct and inverse wavelet transforms, $D_a : g(\tau) \mapsto g(\tau/a)/a$ and $T_t : g(\tau) \mapsto g(\tau - t)$ define the dilation $a \in \mathbb{R}$ and translation $t \in \mathbb{R}$ operations correspondingly. If we select a wavelet with a unit central frequency, it is possible to obtain the physical frequency directly by taking the inverse of the scale: $f = 1/a$.

This approach is powerful and elegant, but is not the only one available for practical applications. Other TFR methods such as the Gabor transform, the S-transform Schimmel and Gallart [2005] or bilinear transforms like the Wigner-Ville Pedersen et al. [2003] or smoothed Wigner-Ville transform can be used as well. The relative performance of time-frequency analysis from different TFR approaches is primarily controlled by the frequency resolution capability that motivated the use of CWT in the present work.

With multicomponent data, one is usually confronted with the issue of separating seismic signals of different polarization characteristics. For instance,

one would like to distinguish between the body waves (P- and S- waves) that are linearly polarized from elliptically polarized Rayleigh waves. Polarization analysis is also used to identify shear wave splitting. Unfortunately, there is no mathematically exact a priori definition for the instantaneous polarization attributes of a multicomponent signal. Therefore any attempts to produce one are usually arbitrary.

Time-frequency representations can be incorporated in polarization analysis Soma et al. [2002], Schimmel and Gallart [2005], Pinnegar [2006]. We proposed several different wavelet based methods for the polarization analysis and filtering.

1.2.1 Polarization Properties for Two-Component Data

Given a signal from three-component record, with $S_x(t)$, $S_y(t)$, and $S_z(t)$ representing the seismic traces recorded in three orthogonal directions, any combination of two orthogonal components can be selected for the polarization analysis: $Z(t) = S_k(t) + iS_m(t)$. Let us consider the instantaneous angular frequency defined as the derivative of the complex spectrum's phase: $\Omega^\pm(t, f) = \pm \partial \arg \mathcal{W}_g^\pm Z(t, f) / \partial t$. Then, near time instant t , each component can be represented as follows:

$$\mathcal{W}_g Z(t + \tau, f) \simeq \mathcal{W}_g^+ Z(t, f) e^{i\Omega^+(t, f)\tau} + \mathcal{W}_g^- Z(t, f) e^{-i\Omega^-(t, f)\tau},$$

which yields the time-frequency spectrum for each of the parameters (see Kulesh et al. [2005b], Diallo et al. [2006b]):

$$\begin{aligned} R(t, f) &= |\mathcal{W}_g^+ Z(t, f)| + |\mathcal{W}_g^- Z(t, f)|/2, \\ r(t, f) &= ||\mathcal{W}_g^+ Z(t, f)| - |\mathcal{W}_g^- Z(t, f)||/2, \\ \theta(t, f) &= \arg[\mathcal{W}_g^+ Z(t, f)\mathcal{W}_g^- Z(t, f)]/2, \\ \Delta\phi(t, f) &= \arg\left(\frac{\mathcal{W}_g^+ Z(t, f) + \mathcal{W}_g^- Z(t, f)^*}{\mathcal{W}_g^+ Z(t, f) - \mathcal{W}_g^- Z(t, f)^*}\right) \bmod \pi, \end{aligned} \tag{1.2}$$

where R is the semi-major axis $R \geq 0$, r is the semi-minor axis $R \geq r \geq 0$, θ is the tilt angle, which is the angle of the semi-major axis with the horizontal axis, $\theta \in (-\pi/2, \pi/2]$ and $\Delta\phi$ is the phase difference between $S_k(t)$ and $S_m(t)$ components.

If we analyze seismic data, an advantage of the method (1.2) is the possibility to perform the complete wave-mode separation/filtering process in the wavelet domain and the ability to provide the frequency dependence of ellipticity, which contains important information on the subsurface structure. With the extension of the polarization analysis to the wavelet domain, we can construct filtering algorithms to separate different wave types based on the instantaneous attributes by a combination of constraints posed on the range of the reciprocal ellipticity $\rho(t, f) = r(t, f)/R(t, f)$ and the tilt angle $\theta(t, f)$ Diallo et al. [2006b].

1.2.2 Polarization Properties for Three-Component Data

Reference Morozov and Smithson [1996] proposed a method based on a variational principle that allows generalization to any number of components, and they briefly addressed the possibility of using the instantaneous polarization attributes for wavefield separation and shear-wave splitting identification. In Diallo et al. [2005], we extended the method of Morozov and Smithson [1996] to the wavelet domain in order to use the instantaneous attributes for filtering and wavefield separation for any number of components. As an example, Pacor et al. [2007] used this method for spectral analysis and multicomponent polarization analyses on the Gubbio Piana (central Italy) recordings to identify the frequency content of the different phases composing the recorded wavefield and to highlight the importance of basin-induced surface waves in modifying the main strong ground-motion parameters.

In more general terms, particle motions captured with three-component recordings can be characterized by a polarization ellipsoid. Several methods are proposed in the literature to introduce such an approximation. They are based on the analysis of the covariance matrix of multicomponent recordings and principal components analysis using singular value decomposition Kanasevich [1981]. In Kulesh et al. [2007a], we extended the covariance method to the time-frequency domain. Following the method, proposed by Diallo et al. [2006a], we use an approximate analytical formula to compute the elements of the covariance matrix $\mathbf{M}(t, f)$ for a time window which is derived from an averaged instantaneous frequency of the multicomponent record:

$$\begin{aligned}
 M_{km}(t, f) &= |\mathcal{W}_g S_k(t, f)| |\mathcal{W}_g S_m(t, f)| \{ \text{sinc}(\Gamma_{km}^-(t, f)) \cos(A_{km}^-(t, f)) \\
 &\quad + \text{sinc}(\Gamma_{km}^+(t, f)) \cos(A_{km}^+(t, f)) \} - \mu_{km} \mu_{mk}, \\
 \Gamma_{km}^\pm(t, f) &= \frac{\Delta t_{km}(t, f)}{2} (\Omega_k(t, f) \pm \Omega_m(t, f)), \\
 A_{km}^\pm(t, f) &= \arg \mathcal{W}_g S_k(t, f) \pm \arg \mathcal{W}_g S_m(t, f), \\
 \Delta t_{km}(t, f) &= \frac{4\pi n}{\Omega_k(t, f) + \Omega_m(t, f)}, \quad n \in \mathbb{N}, \\
 \mu_{kb} &= \Re[\mathcal{W}_g S_k(t, f)] \text{sinc}\left(\frac{\Delta t_{kb}(t, f) \Omega_k(t, f)}{2}\right), \quad k, m = x, y, z,
 \end{aligned} \tag{1.3}$$

where $\text{sinc}(x)$ indicates the sine cardinal function.

The eigenanalysis performed on $\mathbf{M}(t, f)$ yields the principal component decomposition of the energy. Such a decomposition produces three eigenvalues $\lambda_1(t, f) \geq \lambda_2(t, f) \geq \lambda_3(t, f)$ and three corresponding eigenvectors $\mathbf{v}_k(t, f)$ that fully characterize the magnitudes and directions of the principal components of the ellipsoid that approximates the particle motion in the considered time window $\Delta t_{km}(t, f)$:

- the major half-axis $\mathbf{R}(t, f) = \sqrt{\lambda_1(t, f)} \mathbf{v}_1(t, f) / \|\mathbf{v}_1(t, f)\|$;
- the minor half-axis $\mathbf{r}(t, f) = \sqrt{\lambda_3(t, f)} \mathbf{v}_3(t, f) / \|\mathbf{v}_3(t, f)\|$;

- the second minor half-axis $\mathbf{r}_s(t, f) = \sqrt{\lambda_2(t, f)}\mathbf{v}_2(t, f)/\|\mathbf{v}_2(t, f)\|$;
- the reciprocal ellipticity $\rho(t, f) = \|\mathbf{r}_s(t, f)\|/\|\mathbf{R}(t, f)\|$;
- the minor reciprocal ellipticity $\rho_1(t, f) = \|\mathbf{r}(t, f)\|/\|\mathbf{r}_s(t, f)\|$;
- the dip angle $\delta(t, f) = \arctan(\sqrt{v_{1,x}(t, f)^2 + v_{1,y}(t, f)^2}/v_{1,z}(t, f))$;
- the azimuth $\alpha(t, f) = \arctan(v_{1,y}(t, f)/v_{1,x}(t, f))$.

Note, when the instantaneous frequencies are the same for all components, this method produces the same results as those by Morozov and Smithson [1996] in terms of polarization parameters.

1.2.3 Modeling a Wave Dispersion Using a Wavelet Deformation Operator

The second problem in the context of surface wave analysis (especially with high frequency signals) is the robust determination of dispersion curves from multivariate signals. Wave dispersion expresses the phenomenon by which the phase and group velocities are functions of the frequency. The cause of dispersion may be either geometric or intrinsic. For seismic surface waves, the cause of dispersion is of a geometrical nature. Geometric dispersion results from the constructive interferences of waves in bounded or heterogeneous media. Intrinsic dispersion arises from the causality constraint imposed by the Kramers-Krönig relation or from the microstructure properties of material. If the dispersive and dissipative characteristics of the medium are represented by the frequency-dependent wavenumber $k(f)$ and attenuation coefficient $\alpha(f)$, the relation between the Fourier transforms of two propagated signals reads

$$O[\mathcal{D}_{\mathcal{F}}] : \hat{S}(f) \mapsto e^{-i\mathbb{K}(f)D - 2\pi i n} \hat{S}(f),$$

where D is the propagation distance, $n \in \mathbb{N}$ is any integer number and $\mathbb{K}(f)$ is the complex wavenumber, which can be defined by real functions $k(f)$ and $\alpha(f)$ as $\mathbb{K}(f) = 2\pi k(f) - i\alpha(f)$.

In order to analyze the dynamical behavior of multivariate signals using the continuous wavelet transforms it is interesting to investigate a diffeomorphic deformation of the wavelet space. These deformations establish algebra of wavelet pseudodifferential operators acting on signals Xie et al. [2003]. In the most general case, a wavelet deformation operator can be defined as

$$\begin{aligned} O[\mathcal{D}] : S(t) &\mapsto \mathcal{M}_h \mathcal{D} \mathcal{W}_g S(t, f), \quad \mathcal{D} : \mathbb{H} \rightarrow \mathbb{H}, \\ \mathbb{H} &:= \{(t, f) : t \in \mathbb{R}, f > 0\}. \end{aligned}$$

We investigated some practical models that give concreted expression of this deformation operator related to the used dispersion parameters of the medium. Reference Kulesh et al. [2005a] has shown how the wavelet transform of the source and the propagated signals are related through a transformation operator that explicitly incorporates the wavenumber as well as the attenuation factor of the medium:

$$O[\mathcal{D}_W] : \mathcal{W}_g S(t, f) \mapsto e^{-\alpha(f)D} e^{-i\psi_1(f)} \mathcal{W}_g S(t - k'(f)D, f), \quad (1.4)$$

where $\psi_1(f) = 2\pi[k(f) - fk'(f)]D + 2\pi n$.

In the special case, with the assumption that the analyzing wavelet has a linear phase (with time-derivative approximately equal to 2π , as it is the case for the Morlet wavelet, the approximation (1.4) can be written in terms of the phase $C_p(f) = f/k(f)$ and group $C_g(f) = 1/k'(f)$ velocities as Kulesh et al. [2005b]:

$$O[\mathcal{D}_W] : \mathcal{W}_g S(t, f) \mapsto e^{-\alpha(f)D} \left| \mathcal{W}_g S \left(t - \frac{D}{C_g(f)}, f \right) \right| \cdot \exp \left[i \arg \mathcal{W}_g S \left(t - \frac{D}{C_p(f)} - \frac{n}{f}, f \right) \right]. \quad (1.5)$$

The relationship (1.5) has the following interpretation. The group velocity is a function that “deforms” the image of the absolute value of the source signal’s wavelet spectrum, the phase velocity ”deforms” the image of the wavelet spectrum phase, and the attenuation function determines the frequency-dependent real coefficient by which the spectrum is multiplied.

1.2.4 How to Extract the Dispersion Properties from the Wavelet Coefficients?

Equation (1.5) allows us to formulate the ideas how the frequency-dependent dispersion properties can be obtained using the wavelet spectra’ phases of source and propagated signals. To obtain the phase velocities of multi-mode and multivariate signals, we can perform ”frequency-velocity” analysis on the analogy of the frequency-wavenumber method Capon [1969] for a seismogram $S_k(t)$, $k = 1, N$. The main part of this analysis consists of the calculation of correlation spectrum $\mathbf{M}(f, c)$ as follows (see Kulesh et al. [2007b]):

$$\begin{aligned} \mathbf{M}(f, c) &= \int_{t_{min}}^{t_{max}} \left| \sum_{k,m} A_k(\tau, f) A_m^* \left(\tau - \frac{D_{mk}}{c}, f \right) \right| d\tau \\ &= \int_{t_{min}}^{t_{max}} \left| \sum_{k,m} e^{iB_k(\tau, f)} \exp \left(-iB_m \left(\tau - \frac{D_{mk}}{c}, f \right) \right) \right| d\tau, \quad (1.6) \\ A_k(\tau, f) &= \mathcal{W}_g S_k(\tau, f) / |\mathcal{W}_g S_k(\tau, f)|, \quad B_k(\tau, f) = \arg \mathcal{W}_g S_k(\tau, f), \end{aligned}$$

where $[t_{min}, t_{max}]$ indicates the total time range for which the wavelet spectrum was calculated, $c \in [C_p^{min}, C_p^{max}]$ is an unbounded variable corresponding to the phase velocity, A_k is a complex-valued wavelet phase and B_k is a real-valued wavelet phase.

For a given parametrization of wavenumber and attenuation functions, finding an acceptable set of parameters can be thought of as an optimization problem that seeks to minimize a cost function χ^2 and can be formulated as follows:

$$\chi^2(\alpha(f, \mathbf{p}), k(f, \mathbf{q})) \rightarrow \min, \quad \mathbf{p} \in \mathbb{R}^P, \quad \mathbf{q} \in \mathbb{R}^Q,$$

where P is the number of parameters used to model the attenuation $\alpha(f)$ and Q is the number of parameters used to model the wavenumber $k(f)$. \mathbf{p} and \mathbf{q} represent the vectors of parameters describing $\alpha(f)$ and $k(f)$ respectively. This cost function involves a propagator described above.

At this stage we need to distinguish between the case where the analyzed signal consists only of one coherent arrival from the case where it consists of several coherent arrivals. In the former case, the derived functions are meaningful and characterize those analyzed event. However in the latter, these functions cannot be easily interpreted since the signals involved consist of many overlapping arrivals.

If only one single phase is observed in all the traces $S_k(t)$, it will be enough to minimize a cost function that involves some selected seismic traces in order to estimate the attenuation and phase velocity using the modulus and the phase of the wavelet transforms correspondingly, see Holschneider et al. [2005]:

$$\begin{aligned} \chi^2(\mathbf{p}, \mathbf{q}) &= \sum_{m,k} \iint ||\mathcal{W}_g S_k(t, f)| - |\mathcal{D}_W(\mathbf{p}, \mathbf{q}) \mathcal{W}_g S_m(t, f)||^2 dt df, \\ \chi^2(\mathbf{p}, \mathbf{q}) &= \sum_{m,k} \iint |\arg \mathcal{W}_g S_k(t, f) - \arg \mathcal{D}_W(\mathbf{p}, \mathbf{q}) \mathcal{W}_g S_m(t, f)|^2 dt df. \end{aligned} \tag{1.7}$$

The first step will consist of seeking a good initial condition by performing an image matching using the modulus of the wavelet transforms of a pair of traces. The optimization is carried out over the whole frequency range of the signal. In order to reduce the effect of uncorrelated noise in our estimates, it is preferable to use a propagator based on the cross-correlations, see Holschneider et al. [2005].

In the case where the observed signals consist of a mixture of different wave types and modes, a cascade of optimizations in the wavelet domain will be necessary in order to fully determine the dispersion and attenuation characteristics specific to each coherent arrival.

Since the dependence of the cost functions (1.7) on the parameters \mathbf{p} and \mathbf{q} is highly non-linear, each function may have several local minima. To obtain the global minimum that corresponds to the true parameters, a non-linear least-squares minimization method that proceeds iteratively from a reasonable set of initial parameters is required. In the present contribution, we use the Levenberg-Marquardt algorithm Press et al. [1992].

Finally, the obtained dispersion curves (especially phase and group velocities) for defined wave types can be used for the determination of physical and geometrical properties of the subsurface structure. Because of the non-uniqueness of earth models that can be fitted to a given dispersion curve, the inversion for the average shear velocity profile is usually treated as an optimization problem where one tries to minimize the misfit between exper-

imental and theoretical dispersion curves computed for a given earth model that is assumed to best represent the subsurface under investigation.

1.3 The Interplay of Image Registration and Geometry Matching

Image registration is one of the fundamental tools in image processing. It deals with the identification of structural correspondences in different images of the same or of similar objects acquired at different times or with different image devices. For instance, the revolutionary advances in the development of imaging modalities has enabled clinical researchers to perform precise studies of the immense *variability* of human anatomy. As described in the excellent review by Miller, Trouvé and Younes Miller et al. [2002] and the overview article of Grenander and Miller Grenander and Miller [1998], this field aims at automatic detection of anatomical structures and their evaluation and comparison. Different images show corresponding structures at usually nonlinearly transformed positions.

In image processing, registration is often approached as a variational problem. One asks for a deformation ϕ on an image domain Ω which maps structures in the reference image u_R onto corresponding structures in the template image u_T . This leads ill-posed minimization problem if one considers the infinite dimensional space of deformations Brown [1992]. A iterative, multilevel regularization of the descent direction has been investigated in Clarenz et al. [2006]. Alternatively, motivated by models from continuum mechanics, the deformation can additionally be controlled by *elastic stresses* on images regarded as elastic sheets. For example see the early work of Bajcsy and Broit Bajcsy and Broit [1982] and more recent, significant extensions by Grenander and Miller Grenander and Miller [1998]. In Droske and Rumpf [2004] nonlinear elasticity based on polyconvex energy functionals is investigated to ensure a one-to-one image matching. As the image modality differs there is usually no correlation of image intensities at corresponding positions. What still remains, at least partially, is the local geometric image structure or “morphology” of corresponding objects. Viola, Wells et al. Viola and Wells [1997] and Collignon Collignon and et al. [1995] presented an information theoretic approach for the registration of multi-modal images. Here, we consider “morphology” as a geometric entity and will review registration approaches presented in Droske and Ring [2007], Droske and Rumpf [2004, 2005].

Obviously, geometry matching is also a widespread problem in computer graphics and geometric modeling Gu and Vemuri [2004]. E.g. motivated by the ability to scan geometry with high fidelity, a number of approaches have been developed in the graphics literature to bring such scans into correspondence Blanz and Vetter [1999], Lee et al. [1999]. Given a reference surface \mathcal{M}_R and a template surface \mathcal{M}_T a particular emphasize is on the proper alignment

of curved features and the algorithmic issues associated with the management of irregular meshes and their effective overlay. Here, we will describe an image processing approach to the nonlinear elastic matching of surface patches Litke et al. [2005]. It is based on a proper variational parametrization method Clarenz et al. [2004] and on the matching of surface characteristics encoded as images u_R and u_T on flat parameter domains ω_R and ω_T , respectively. Here, it is particularly important to take into account of the metric distortion, to ensure a physically reasonable matching of the actual surfaces \mathcal{M}_R and \mathcal{M}_T .

1.3.1 The Geometry of Images

In mathematical terms, two images $u, v : \Omega \rightarrow \mathbb{R}$ with $\Omega \subset \mathbb{R}^d$ for $d = 2, 3$ are called morphologically equivalent, if they only differ by a change of contrast, i.e., if $u(x) = (\beta \circ v)(x)$ for all $x \in \Omega$ and for some monotone function $\beta : \mathbb{R} \rightarrow \mathbb{R}$. Obviously, such a contrast modulation does not change the order and the shape of super level sets $l_c^+[u] = \{x : u(x) \geq c\}$. Thus, image morphology can be defined as the upper topographic map, defined as the set of all these sets $\text{morph}[u] := \{l_c^+[u] : c \in \mathbb{R}\}$. Unfortunately, this set based definition is not feasible for a variational approach and it does not distinguish between edges and level sets in smooth image regions. Hence, in what follows, we derive an alternative notion and consider image functions $u : \Omega \rightarrow \mathbb{R}$ in SBV Ambrosio et al. [2000] - by definition L^1 functions, whose derivative Du is a vector-valued Radon measure with vanishing Cantor part. We consider the usual splitting $Du = D^{ac}u + D^j u$ Ambrosio et al. [2000], where $D^{ac}u$ is the regular part, which is the usual image gradient apart from edges and absolutely continuous with respect to the Lebesgue measure \mathcal{L} , and a singular part $D^j u$, which represents the jump and is defined on the jump set J , which consists of the edges of the image. We denote by n^j the vector valued measure representing the normal field on J . Obviously, n^j is a morphological invariant. For the regular part of the derivative we adopt the classical gradient notion $\nabla^{ac}u$ for the \mathcal{L} density of $D^{ac}u$, i.e., $D^{ac}u = \nabla^{ac}u \mathcal{L}$ Ambrosio et al. [2000]. As long as it is defined, the normalized gradient $\nabla^{ac}u(x) / \|\nabla^{ac}u(x)\|$ is the outer normal on the upper topographic set $l_{u(x)}^+[u]$ and thus again a morphological quantity. It is undefined on the flat image region $F[u] := \{x \in \Omega : \nabla^{ac}u(x) = 0\}$. We introduce n^{ac} as the normalized regular part of the gradient $n^{ac} = \chi_{\Omega \setminus F[u]} \nabla^{ac}u / \|\nabla^{ac}u\|$. We are now able to redefine the morphology $\text{morph}[u]$ of an image u as a unit length vector valued Radon measure on Ω with $\text{morph}[u] = n^{ac} \mathcal{L} + n^s$. We call $n^{ac} \mathcal{L}$ the regular morphology or Gauss map (GM) and n^s the singular morphology. In the next section, we aim to measure congruence of two image morphologies with respect to a matching deformation making explicit use of this decomposition.



Fig. 1.1. The morphological registration is demonstrated for a test case. From left to right the reference image u_R , the contrast modulated and artificially deformed template image u_T , the jump set J_T in the template image u_T (represented by a phase field function), the deformation ϕ^{-1} of the template image visualized with a deformed underlying checkerboard, and finally the registered template image $u_T \circ \phi$ are displayed

1.3.2 Matching Image Morphology

Let us suppose that an initial template image u_T^0 and an initial reference image u_R^0 are given on an image domain Ω . Both images are assumed to be noisy. We aim for a simultaneous robust identification of smoothed and structural enhanced representations $u_T, u_R \in SBV$ and a deformation ϕ , which properly matches the underlying image morphologies, such that $\text{morph}[u_T \circ \phi] = \text{morph}[u_R]$. To phrase this in terms a variational approach we treat the two different components of the morphology separately.

Matching the Singular Morphology

We aim for a deformation ϕ a proper matching of the singular morphologies requesting that $\phi(J_R) = J_T$ for the edge sets $J_R := J_{u_R}$ and $J_T := J_{u_T}$. Now, we ask for a simultaneous edge segmentation, denoising and matching of images in terms of a Mumford Shah approach jointly applied to both images and linked via the unknown elastic deformation. I.e., we consider as set of unknowns u_T, u_R, J_T and ϕ . For the template image we take into account the usual Mumford Shah approach and define the energy

$$E_{MS}^T[u_T, J_T] = \frac{1}{2} \int_{\Omega} (u_T - u_T^0)^2 \, d\mathcal{L} + \frac{\mu}{2} \int_{\Omega \setminus J_T} \|\nabla u_T\|^2 \, d\mathcal{L} + \eta \mathcal{H}^{d-1}(S_T)$$

with $\mu, \eta > 0$. For the reference image we make use of our correspondence assumption and define

$$E_{MS}^R[u_R, J_T, \phi] = \frac{1}{2} \int_{\Omega} (u_R - u_R^0)^2 \, d\mathcal{L} + \frac{\mu}{2} \int_{\Omega \setminus \phi^{-1}(J_T)} \|\nabla u_R\|^2 \, d\mathcal{L},$$

where the \mathcal{H}^{d-1} -measure of J_R is supposed to be implicitly controlled by the \mathcal{H}^{d-1} -measure of J_T and a smooth deformation ϕ . Hence, we omit the corresponding energy term here. Finally, the energy for the joint Mumford Shah segmentation and matching model in the reference and the template

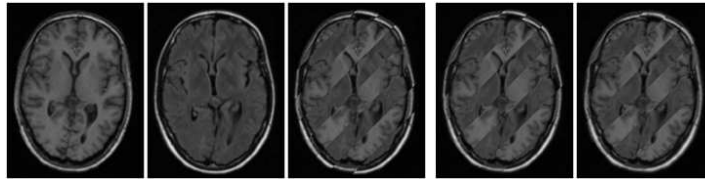


Fig. 1.2. The registration of FLAIR and T1-weighted magnetic resonance brain images is considered. From left to right: the reference T1 weighted MR image u_R , the template FLAIR image u_T , the initial mismatch (with alternating stripes from u_T and u_R), and in the same fashion results for a registration only of the regular morphology and finally for the complete energy are shown

image is given by $E_{MS}[u_R, u_T, S_T, \phi] = E_{MS}^T[u_T, J_T] + E_{MS}^R[u_R, J_T, \phi]$. So far, the deformation ϕ is needed only on the singularity set S_T and thus it is highly under determined.

Matching the Regular Morphology

The regular image morphology consists of the normal field n^{ac} . Given regularized representations u_T and u_R of noisy initial images we observe a perfect match of the corresponding regular morphologies, if the deformation of the reference normal field $n_R^{ac} := \nabla^{ac} u_R / \|\nabla^{ac} u_R\|$ coincides with the template normals field $n_T^{ac} := \nabla^{ac} u_T / \|\nabla^{ac} u_T\|$ at the deformed position. In fact, all level sets of the pull back template image $u_T \circ \phi$ and the reference image u_R would then be nicely aligned. In the context of a linear mapping A normals deformed with the inverse transpose A^{-T} . Thus, we obtain the deformed reference normal $n_R^{ac, \phi} = \text{Cof } D\phi \nabla^{ac} u_R / \|\text{Cof } D\phi \nabla^{ac} u_R\|$, where $\text{Cof } A := \det A A^{-T}$ and ask for a deformation $\phi : \Omega \rightarrow \mathbb{R}^d$, such that $n_T^{ac} \circ \phi = n_R^{ac, \phi}$. This can be phrased in terms of an energy integrand $g_0 : \mathbb{R}^d \times \mathbb{R}^d \times \mathbb{R}^{d,d} \rightarrow \mathbb{R}_0^+$, which is zero-homogeneous in the first two arguments as long as they both do not vanish and zero elsewhere. It measures the misalignment of directions of vectors on \mathbb{R}^d . For instance we might define

$$g_0(w, z, A) := \gamma \left\| \left(\mathbb{1} - \frac{w}{\|w\|} \otimes \frac{w}{\|w\|} \right) \frac{\text{Cof } Az}{\|\text{Cof } Az\|} \right\|^m$$

for $w, z \neq 0$, with $\gamma > 0$ and $m \geq 2$, $a \otimes b = ab^T$. Based on this integrand we finally define a Gauss map registration energy

$$E_{GM}[u_T, u_R, \phi] = \int_{\Omega} g_0(D^{ac} u_T \circ \phi, D^{ac} u_R, \text{Cof } D\phi) \, d\mathcal{L}.$$

For the analytical treatment of the corresponding variational problem we refer to Droske and Rumpf [2004].

In a variational setting neither the matching energy for the singular morphology nor the one for the regular morphology uniquely identify the deformation ϕ . Indeed, the problem is still ill-posed. For instance, arbitrary

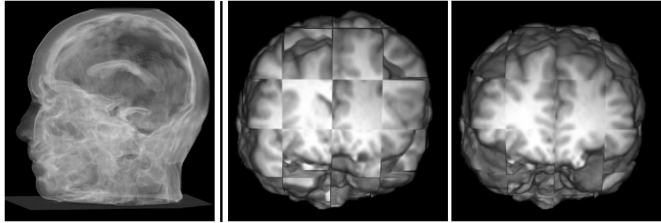


Fig. 1.3. On the left the 3D phasefield corresponding to the edge set in the an MR image is shown. Furthermore, the matching of two MR brain images of different patients is depicted. We use a volume renderer based on ray casting (VTK) for a 3D checkerboard with alternating boxes of the reference and the pull back of the template image to show the initial mismatch of MR brain images of two different patients (middle) and the results of our matching algorithm (right)

reparametrizations of the level sets ∂I_c^+ or the edge set J , and an exchange of level sets induced by the deformation do not change the energy. Thus, we have to regularize the variational problem. On the background of elasticity theory Ciarlet [1988], we aim to model the image domain as an elastic body responding to forces induced by the matching energy. Let us consider the deformation of length, volume and for $d = 3$ also area under a deformation ϕ , which is controlled by $D\phi / \|D\phi\|$, $\det D\phi$, and $\text{Cof } D\phi / \|\text{Cof } D\phi\|$, respectively. In general, we consider a so called polyconvex energy functional

$$E_{reg}[\phi] := \int_{\Omega} W(D\phi, \text{Cof } D\phi, \det d\phi) d\mathcal{L}, \quad (1.8)$$

where $W : \mathbb{R}^{d,d} \times \mathbb{R}^{d,d} \times \mathbb{R} \rightarrow \mathbb{R}$ is supposed to be convex. In particular, a suitable built-in penalization of volume shrinkage, i. e., $W(A, C, D) \xrightarrow{D \rightarrow 0} \infty$, enables us to ensure bijectivity of the deformation (cf. Ball [1981]) and one-to-one image matches. For details we refer to Droske and Rumpf [2004]. With respect to the algorithmical realization we take into account a phase field approximation of the Mumford Shah energy E_{MS} picking up the approach by Ambrosio and Tortorelli Ambrosio and Tortorelli [1992]. Thereby, the edge set J_T in the template image will be represented by a phase field function v , hence $v \circ \phi$ can be regarded as the phase field edge representation in the reference image Droske and Rumpf [2005]. As an alternative a shape optimization approach based on level sets can be used Droske and Ring [2007]. Results of the morphological matching algorithm are depicted in Fig. 1.1, Fig. 1.2 and Fig. 1.3.

1.3.3 Images Encoding Geometry

So far, we have extensively discussed the importance of geometry encoded in images for the purpose of morphological image matching. Now, we will discuss

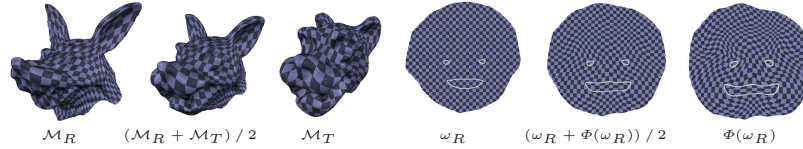


Fig. 1.4. Large deformations are often needed to match surfaces that have very different shapes. A checkerboard is texture mapped onto the first surface as it morphs to the second surface (top). The matching deformation shown in the parameter domain (bottom) is smooth and regular, even where the distortion is high (e.g., around the outlines of the mouth and eyes)

how surface geometry can be encoded in images and how to make use of this encoding for surface matching purposes. Consider a smooth surface $\mathcal{M} \subset \mathbb{R}^3$, and suppose $x : \omega \rightarrow \mathcal{M}$; $\xi \mapsto x(\xi)$ is a parameterization of \mathcal{M} on a parameter domain ω . The metric $g = Dx^T Dx$ is defined on ω , where $Dx \in \mathbb{R}^{3,2}$ is the Jacobian of the parameterization x . It acts on tangent vectors v, w on the parameter domain ω with $(gv) \cdot w = Dxv \cdot Dxw$ and describes how length, area and angles are distorted under the parameterization x . This distortion is measured by the inverse metric $g^{-1} \in \mathbb{R}^{2,2}$. In fact, $\sqrt{\text{tr } g^{-1}}$ measures the average change of length of tangent vectors under the mapping from the surface onto the parameter plane, whereas $\sqrt{\det g^{-1}}$ measures the corresponding *change of area*. As a surface classifier the mean curvature on \mathcal{M} can be considered as a function h on the parameter domain ω . Similarly a feature set $\mathcal{F}_{\mathcal{M}}$ on the surface \mathcal{M} can be represented by a set \mathcal{F} on ω . Examples for feature sets for instance on facial surfaces are particularly interesting sets such as the eye holes, the center part of the mouth, or the symmetry line of a suitable width between the left and the right part of the face. Finally, surface textures \mathcal{T} usually live on the parameter space. Hence, the quadruple $(x, h, \mathcal{F}, \mathcal{T})$ can be regarded as an encoding of surface geometry in a geometry image on the parameter domain ω . The quality of a parameterization can be described via a suitable distortion energy $E_{\text{param}}[x] = \int_{x^{-1}(\mathcal{M})} W(\text{tr}(g^{-1}), \det g^{-1}) dx$. For details on the optimization of the parametrization based on this variational approach we refer to Clarenz et al. [2004].

1.3.4 Matching Geometry Images

Let us now consider a reference surface patch \mathcal{M}_R and a template patch \mathcal{M}_T to be matched, where geometric information is encoded via two initially fixed parameter maps x_R and x_T on parameter domains ω_R and ω_T . In what follows we always use indices R and T to distinguish quantities on the reference and the template parameter domain. First, let us consider a one-to-one deformation $\phi : \omega_R \rightarrow \omega_T$ between the two parameter domains. This induces a deformation between the surface patches $\phi_{\mathcal{M}} : \mathcal{M}_R \rightarrow \mathcal{M}_T$ defined by $\phi_{\mathcal{M}} := x_T \circ \phi \circ x_R^{-1}$. Now let us focus on the distortion from the surface \mathcal{M}_R onto the surface \mathcal{M}_T .

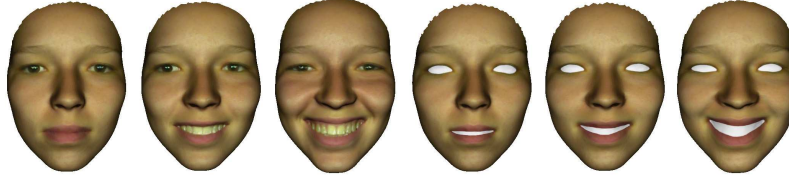


Fig. 1.5. Morphing through keyframe poses A, B, C is accomplished through pairwise matches $A \rightarrow B$ and $B \rightarrow C$. The skin texture from A is used throughout. Because of the close similarity in the poses, one can expect the intermediate blends A', B', C' to correspond very well with the original keyframes A, B, C , respectively

In elasticity, the distortion under an elastic deformation ϕ is measured by the Cauchy-Green strain tensor $D\phi^T D\phi$. Properly incorporating the metrics g_R and g_T we can adapt this notion and obtain the Cauchy Green tangential distortion tensor $\mathcal{G}[\phi] = g_R^{-1} D\phi^T (g_T \circ \phi) D\phi$, which acts on tangent vectors on the parameter domain ω_R . As in the parameterization case, one observes that $\sqrt{\text{tr} \mathcal{G}[\phi]}$ measures the average change of length of tangent vectors from \mathcal{M}_R when being mapped to tangent vectors on \mathcal{M}_T and $\sqrt{\det \mathcal{G}[\phi]}$ measures the change of area under the deformation ϕ_M . Thus, $\text{tr} \mathcal{G}[\phi]$ and $\det \mathcal{G}[\phi]$ are natural variables for an energy density in a variational approach measuring the tangential distortion, i.e. we define an energy of the type

$$E_{reg}[\phi] = \int_{\omega_R} W(\text{tr} \mathcal{G}[\phi], \det \mathcal{G}[\phi]) \sqrt{\det g_R} d\xi.$$

When we press a given surface \mathcal{M}_R into the thin mould of the surface \mathcal{M}_T , a second major source of stress results from the bending of normals. A simple thin shell energy reflecting this is given by

$$E_{bend}[\phi] = \int_{\omega_R} (h_T \circ \phi - h_R)^2 \sqrt{\det g_R} d\xi.$$

Frequently, surfaces are characterized by similar geometric or texture features, which should be matched in a way which minimizes the difference of the deformed reference set $\phi_M(\mathcal{F}_{\mathcal{M}_R})$ and the corresponding template set $\mathcal{F}_{\mathcal{M}_T}$. Hence, we consider a third energy

$$E_{\mathcal{F}}[\phi] = \mu \int_{\omega_R} \chi_{\mathcal{F}_R} \chi_{\phi^{-1}(\mathcal{F}_T)} \sqrt{\det g_R} + \mu \int_{\omega_T} \chi_{\phi(\mathcal{F}_R)} \chi_{(\mathcal{F}_T)} \sqrt{\det g_T}.$$

Usually, we cannot expect that $\phi_M(\mathcal{M}_R) = \mathcal{M}_T$. Therefore, we must allow for a partial matching. For details on this and on the numerical approximation we refer to Litke et al. [2005]. Fig. 1.4 and 1.5 show two different application of the variational surface matching method.

1.4 An Optimal Control Problem in Medical Image Processing

In this section we consider the problem of creating a “natural” movie which interpolates two given images showing essentially the same objects. In many situations, these objects are not at the same position or - more importantly - may be out-of-focus and blurred in one image while being in focus and sharp in the other. This description may be appropriate for frames in movies but also for different versions of a mammogram emphasizing coarse and fine details, respectively. The problem is to create an interpolating movie from these images which is perceived as “natural”. In this context, we specify “natural” according to the following requirements. On the one hand, objects from the initial image should move smoothly to the corresponding object in the final image. On the other hand, the interpolation of an object which is blurred in the initial image and sharp in the final image (or vice versa) should be across different stages of sharpness, i.e. , the transition is also required to interpolate between different scales.

As a first guess to solve this problem, one can either try to use an existing morphing algorithm or to interpolate linearly between the two images. However, morphing methods are based on detecting matching landmarks in both images. They are not applicable here, since we are particularly interested in images containing objects, which are not present or heavily diffused in the initial image but appear with a detailed structure in the final image. Hence, there are no common landmarks for those objects. Mathematically speaking, it is difficult or impossible to match landmark points for an object which is given on a coarse and fine scale, respectively. Also linear interpolation between initial and final image does not create a natural image sequence, since it does not take the scale sweep into account, i.e. , all fine scale are appearing immediately rather than developing one after another.

Hence, more advanced methods have to be employed. In this article we show a solution of this interpolation problem based on optimal control of partial differential equations.

To put the problem in mathematical terms, we start with a given image y_0 assumed to be a function on $\Omega =]0, 1[^2$. Under the natural assumption of finite-energy images, we model them as functions in $L^2(\Omega)$. The goal is to produce a movie (i.e. a time-dependent function) $y : [0, 1] \rightarrow L^2(\Omega)$ such that appropriate mathematical implementations of the above conditions are satisfied.

1.4.1 Modeling as an Optimal Control Problem

Parabolic partial differential equations are a widely used tool in image processing. Diffusion equations like the heat equation Witkin [1983], the Perona-Malik equation Perona and Malik [1988] or anisotropic equations Weickert [1998] are used for smoothing, denoising and edge enhancing.

A smoothing of a given image $y_0 \in L^2(\Omega)$ can for example be done by solving the heat equation

$$\begin{aligned} y_t - \Delta y &= 0 \quad \text{in }]0, 1[\times \Omega \\ y_\nu &= 0 \quad \text{on }]0, 1[\times \partial\Omega \\ y(0) &= y_0, \end{aligned}$$

where y_ν stands for the normal derivative, i.e. we impose homogeneous Neumann boundary conditions. The solution $y : [0, 1] \rightarrow L^2(\Omega)$ gives a movie which starts at the image y_0 and becomes smoother with time t . This evolution is also called scale space and is analyzed by the image processing community in detail since the 1980s. Especially the heat equation does not create new features with increasing time, see e.g. Florack and Kuijper [2000] and the references therein. Thus, it is suitable for fading from fine to coarse scales.

The opposite direction, the sweep from coarse to fine scales, however, is not modeled by the heat equation. Another drawback of this PDE is that generally, all edges of the initial image will be blurred. To overcome this problem, the equation is modified such that it accounts for the edges and allows the formation of new structures. The isotropic diffusion is replaced with the degenerate diffusion tensor given by

$$D_p^2 = \left(I - \sigma(|p|) \frac{p}{|p|} \otimes \frac{p}{|p|} \right), \quad (1.9)$$

where the vector field $p :]0, 1[\times \Omega \rightarrow \mathbb{R}^d$ with $|p| \leq 1$ describes the edges of the interpolating sequence and $\sigma : [0, 1] \rightarrow [0, 1]$ is an edge-intensity function. The special feature of this tensor is that it is allowed to degenerate for $|p| = 1$, blocking the diffusion in the direction of p completely.

Consequently, the degenerate diffusion tensor D_p^2 can be used for the preservation of edges. Additionally, in order to allow brightness changes and to create fine-scale structures, a source term u is introduced. The model under consideration then reads as:

$$\begin{aligned} y_t - \operatorname{div} (D_p^2 \nabla y) &= u \quad \text{in }]0, 1[\times \Omega \\ \nu \cdot D_p^2 \nabla y &= 0 \quad \text{on }]0, 1[\times \partial\Omega \\ y(0) &= y_0. \end{aligned} \quad (1.10)$$

The above equation is well-suited to model a sweep from an image y_0 to an image y_1 representing objects on different scale. Hence, we take the image y_0 as initial value. To make the movie y end at a certain coarse scale image y_1 instead of the endpoint $y(1)$ which is already determined through (y_0, u, p) , we propose the following optimal control problem:

$$\begin{aligned}
& \text{Minimize } J(y, u, p) = \frac{1}{2} \int_{\Omega} |y(1) - y_1|^2 \, dx + \int_0^1 \int_{\Omega} \frac{\lambda_1}{2} |u|^2 + \lambda_2 \sigma(|p|) \, dx \, dt \\
& \text{subject to } \begin{cases} y_t - \operatorname{div}(D_p^2 \nabla y) = u & \text{in }]0, 1[\times \Omega \\ \nu \cdot D_p^2 \nabla y = 0 & \text{on }]0, 1[\times \partial\Omega \\ y(0) = y_0. \end{cases} \quad (1.11)
\end{aligned}$$

In other words, the degenerate diffusion process is forced to end in y_0 with the help of a heat source u and the edge field p and such that the energy for u and the edge-intensity $\sigma(|p|)$ becomes minimal.

1.4.2 Solution of the Optimal Control Problem

The minimization of the functional (1.11) is not straightforward. An analytical treatment of the minimization problem involves a variety of mathematical tasks. First, an appropriate weak formulation for (1.10) has to be found for which existence and uniqueness of solutions can be proven. Second, we have to ensure that a minimizer of a possibly regularized version of (1.11) exists. The main difficulty in these two points is to describe the influence of the parameter p in the underlying degenerate parabolic equation which control where the position and evolution of the edges in the solution. A general approach for minimizing Tikhonov functionals such as (1.11) by a generalized gradient method can be found in Bredies et al. [2008].

The Solution of the PDE

The solution of diffusion equations which are uniformly elliptic is a classical task. The situation changes when degenerate diffusion tensors like (1.9) are considered. In the following we fix an edge field p and examine the PDE (1.10) only with respect to (u, y_0) which is now linear. Here, when considering weak solutions, the choice of $L^2(0, 1; H^1(\Omega))$ for the basis of a solution space is not sufficient. This has its origin in one of the desired features of the equation: In order to preserve and create edges, which correspond to discontinuities in y with respect to the space variable, the diffusion tensor is allowed to degenerate. Such functions cannot be an element of $L^2(0, 1; H^1(\Omega))$. Hence, spaces adapted to the degeneracies have to be constructed by the formal closure with respect to a special norm (also see Oleřnik and Radkevič [1973] for a similar approach):

$$\mathcal{V}_p = L^2(0, 1; H^1(\Omega))|_{\|\cdot\|_{\mathcal{V}_p}}^{\sim}, \quad \|y\|_{\mathcal{V}_p} = \left(\int_0^1 \int_{\Omega} |y|^2 + |D_p \nabla y|^2 \, dx \, dt \right)^{1/2}.$$

Elements y can be thought of square-integrable functions for which formally $D_p \nabla y \in L^2(0, 1; L^2(\Omega))$. One can moreover see that functions which admit

discontinuities where $|p| = 1$ are indeed contained in \mathcal{V}_p . In the same manner, the solution space

$$W_p(0, 1) = \{y \in \mathcal{AC}(0, 1; H^1(\Omega)) \mid \|y\|_{W_p} < \infty\} \Big|_{\|\cdot\|_{W_p}}^{\sim},$$

$$\|y\|_{W_p} = (\|y\|_{\mathcal{V}_p}^2 + \|y_t\|_{\mathcal{V}_p^*}^2)^{1/2}.$$

A weak formulation of (1.10) then reads as: Find $y \in \mathcal{V}_p$ such that

$$-\langle z_t, y \rangle_{\mathcal{V}_p^* \times \mathcal{V}_p} + \langle D_p \nabla y, D_p \nabla z \rangle_{L^2} = \langle y_0, z(0) \rangle_{L^2} + \langle u, z \rangle_{L^2} \quad (1.12)$$

for all $z \in W_p(0, 1)$ with $z(T) = 0$. One can prove that a unique solution exists in this sense.

Theorem 1.1. *For $p \in L^\infty([0, 1] \times \Omega, \mathbb{R}^d)$ with $\|p\|_\infty \leq 1$, $u \in L^2(0, 1; L^2(\Omega))$ and $y_0 \in L^2(\Omega)$, there exists a unique solution of (1.12) in $W_p(0, T)$ with*

$$\|y\|_{W_p}^2 \leq C(\|u\|_2^2 + \|y_0\|_2^2)$$

where C is also independent of p .

Proof. A solution can be obtained, for example with Lions' projection theorem or with Galerkin approximations. Both approaches yield the same solution in $W_p(0, 1)$, whose uniqueness can be seen by a monotonicity argument. However, other solutions may exist in the slightly larger space

$$\bar{W}_p(0, 1) = \{y \in \mathcal{V}_p \mid y_t \in \mathcal{V}_p^*\}, \quad \|y\|_{\bar{W}_p} = \|y\|_{W_p},$$

see Bredies [2007] for details. \square

Unfortunately, for each p , the solution space may be different and, in general, no inclusion relation holds. This complicates the analysis of the solution operator with respect to p in a profound way.

But fortunately, the spaces $W_p(0, 1)$ still possess the convenient property that each $W_p(0, 1) \hookrightarrow \mathcal{C}([0, 1]; L^2(\Omega))$ with embedding constant independent of p . So, the solution operator

$$\mathcal{S} : L^2(0, 1; L^2(\Omega)) \times \{\|p\|_\infty \leq 1\} \rightarrow \mathcal{C}([0, 1]; L^2(\Omega)), \quad (u, p) \mapsto y$$

is well-defined and bounded on bounded sets.

Examining the continuity of \mathcal{S} , a bounded sequence $\{u_l\}$ and arbitrary $\{p_l\}$ have, up to a subsequence, weak- and weak*-limits u and p . Since $\mathcal{C}([0, 1]; L^2(\Omega))$ is not reflexive, we cannot assure weak convergence of the bounded sequence $\{y_k\}$, but it is possible to show that a weak limit exists y in the slightly larger space $\mathcal{C}^*([0, 1]; L^2(\Omega))$ in which point-evaluation is still possible, again see Bredies [2007] for details. The problem now is to show that the solution operator is closed in the sense that $\mathcal{S}(u, p) = y$.

Characterization of the Solution Spaces

One difficulty in examining the varying solution spaces \mathcal{V}_p is the definition as a closure with respect to a norm which depends on p , resulting in equivalence classes of Cauchy sequences. A more intuitive description of the \mathcal{V}_p is given in terms of special weak differentiation notions, as it is demonstrated in the following. In particular, this allows to describe the behavior of the solution operator \mathcal{S} with respect to p .

For $w \in H^{1,\infty}(\Omega)$ and $q \in H^{1,\infty}(\Omega, \mathbb{R}^d)$, the *weak weighted derivative* and *weak directional derivative* of y are the functions, denoted by $w\nabla y$ and $\partial_q y$, respectively, satisfying

$$\begin{aligned} \int_{\Omega} (w\nabla y) \cdot z \, dx &= - \int_{\Omega} y (w \operatorname{div} z + \nabla w \cdot z) \, dx \quad \text{for all } z \in \mathcal{C}_0^\infty(\Omega, \mathbb{R}^d) \\ \int_{\Omega} \partial_q y z \, dx &= - \int_{\Omega} y (z \operatorname{div} q + \nabla z \cdot q) \, dx \quad \text{for all } z \in \mathcal{C}_0^\infty(\Omega). \end{aligned}$$

With the help of these notions, a generalization of the well-known weighted Sobolev spaces Kufner [1980] can be introduced, the *weighted and directional Sobolev spaces* associated with a weight $w \in H^{1,\infty}(\Omega)$ and directions $q_1, \dots, q_K \in H^{1,\infty}(\Omega, \mathbb{R}^d)$:

$$\begin{aligned} H_{w, \partial_{q_1}, \dots, \partial_{q_K}}^2(\Omega) &= \{y \in L^2(\Omega) \mid w\nabla y \in L^2(\Omega, \mathbb{R}^d), \partial_{q_1} y, \dots, \partial_{q_K} y \in L^2(\Omega)\} \\ \|y\|_{H_{w, \partial_{q_1}, \dots, \partial_{q_K}}^2} &= \left(\|y\|_2^2 + \|w\nabla y\|_2^2 + \sum_{k=1}^K \|\partial_{q_k} y\|_2^2 \right)^{1/2}. \end{aligned}$$

These spaces generalize weighted Sobolev spaces in the sense that ∇y does not necessarily exist for elements in $H_w^2(\Omega)$ and that $w = 0$ is allowed on non-null subsets of Ω .

The gain now is that the following weak closedness properties can be established:

$$\left. \begin{array}{l} y_l \rightharpoonup y \\ w_l \nabla y_l \rightharpoonup \theta \\ \partial_{q_{k,l}} y_l \rightharpoonup v_k \end{array} \right\} \text{ and } \left. \begin{array}{l} w_l \xrightarrow{*} w \\ q_{k,l} \xrightarrow{*} q_k \\ \operatorname{div} q_{k,l} \rightarrow \operatorname{div} q_k \\ \text{pointwise a.e.} \end{array} \right\} \Rightarrow \begin{cases} w\nabla y = \theta \\ \partial_{q_k} y = v_k. \end{cases} \quad (1.13)$$

Such a result is the key to prove that the solution operator \mathcal{S} possesses appropriate closedness properties.

The construction of the weighted and directional weak derivative as well as the associated spaces can also be carried out for the time-variant case, resulting in spaces $\mathcal{H}_{w, \partial_{q_1}, \dots, \partial_{q_K}}^2$. Splitting the diffusion tensor (1.9) then into a weight and direction as follows

$$w = \sqrt{1 - \sigma(|p|)}, \quad q = \begin{pmatrix} 0 & -1 \\ 1 & 0 \end{pmatrix} \frac{\sqrt{\sigma(|p|)}}{|p|} p$$

yields $D_p^2 = w^2 I + q \otimes q$, so $\nabla z \cdot D_p^2 \nabla y = w \nabla y \cdot w \nabla z + \partial_q y \partial_q z$. This gives an equivalent weak formulation in terms of weak weighted and directional derivatives.

Theorem 1.2. *For $\|p(t)\|_{H^{1,\infty}} \leq C$ a.e. and $|p| < 1$ on $]0, 1[\times \partial\Omega$ follows that $\mathcal{V}_p = \mathcal{H}_{w,q}^2$ and $W_p(0, 1) = \bar{W}_p(0, 1)$. A $y \in \mathcal{V}_p$ is the unique solution of (1.12) if and only if*

$$-\langle z_t, y \rangle_{\mathcal{H}_{w,q}^{2*} \times \mathcal{H}_{w,q}^2} + \langle w \nabla y, w \nabla z \rangle_{L^2} + \langle \partial_q y, \partial_q z \rangle_{L^2} = \langle y_0, z(0) \rangle_{L^2} + \langle u, z \rangle_{L^2} \quad (1.14)$$

for each $z \in W_p(0, 1)$, $z_t \in L^2(0, 1; L^2(\Omega))$ and $z(T) = 0$.

Proof. For the proof and further details we again refer to Bredies [2007]. \square

Existence of Optimal Solutions

The characterization result of Theorem 1.2 as well as time-variant versions of the closedness property (1.13) are the crucial ingredients to obtain existence of solutions for a regularized version of (1.11).

Theorem 1.3. *Let \mathcal{P} a weak*-compact set such that each $p \in \mathcal{P}$ satisfies the prerequisites of Theorem 1.2. The control problem*

$$\begin{aligned} \min_{\substack{u \in L^2(0,1;L^2(\Omega)) \\ p \in \mathcal{P}}} & \frac{\|y(1) - y_1\|_2^2}{2} + \lambda_1 \|u\|_2^2 + \lambda_2 \int_0^T \int_{\Omega} \sigma(|p|) \, dx \, dt \\ & + \mu_1 \text{tv}^*(p) + \mu_2 \operatorname{ess\,sup}_{t \in [0,1]} \text{TV}(\nabla p(t)) \\ \text{subject to} & \begin{cases} y_t - \operatorname{div}(D_p^2 \nabla y) = u & \text{in }]0, 1[\times \Omega \\ \nu \cdot D_p^2 \nabla y = 0 & \text{on }]0, 1[\times \partial\Omega \\ y(0) = y_0. \end{cases} \end{aligned}$$

possesses at least one solution (u^*, p^*) . Here, tv^* and TV denote the semi-variation with respect to t and the total variation, respectively.

Proof. The proof can roughly be sketched as follows, see Bredies [2007] for a rigorous version. For a minimizing sequence (y_l, u_l, p_l) , one obtains weak- and weak*-limits (y^*, u^*, p^*) according to the compactness stated above. Theorem 1.2 gives weakly convergent sequences $w_l \nabla y_l$ and $\partial_{q_l} y_l$ as well as the alternative weak formulation (1.14). The total-variation regularization terms then ensure the applicability of closedness properties analog to (1.13), so passing to the limit in (1.14) yields that $y^* \in \bar{W}_{p^*}(0, 1)$ is the unique solution associated with (u^*, p^*) . Finally, with a lower-semicontinuity argument, the optimality is verified. \square

Having established the existence of at least one minimizing element, one can proceed to derive an optimality system based on first-order necessary conditions (which is possible for $\|p\| < 1$). Furthermore, numerical algorithms for the optimization of the discrete version of (1.11) can be implemented, see Fig. 1.6 for an illustration of the proposed model.

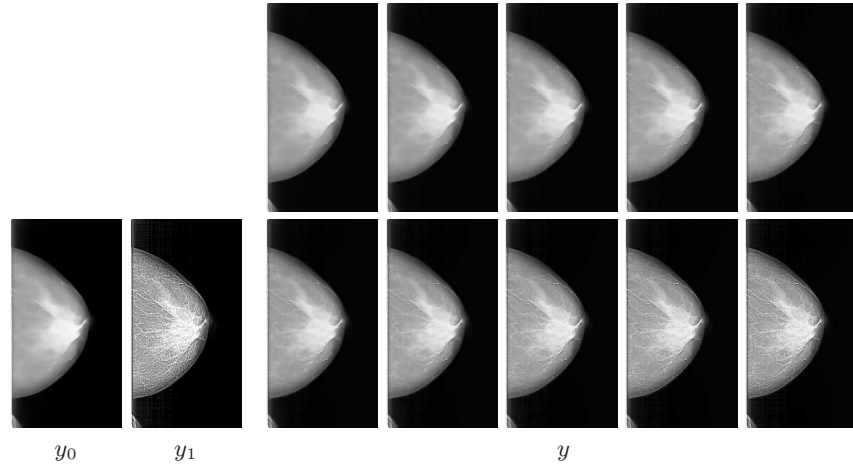


Fig. 1.6. Illustration of an interpolating sequence generated by solving the proposed optimal control problem. The two leftmost images depict y_0 and y_1 , respectively (a coarse- and fine-scale version of a mammography image), while some frames of the optimized image sequence can be seen on the right

1.5 Restoration and Post Processing of Optical Flows

The estimation of motion in image sequence has gained wide spread importance in a number of scientific applications stemming from diverse fields such as environmental and life-sciences. From optical imaging systems, non-invasive techniques are feasible, a prerequisite for accurate measurements. For analyzing transport processes, the estimation of motion or optical flow plays a central role. Equally, in engineering applications the estimation of motion from image sequences is not only important in fluid dynamics but can also be used in novel products such as driver assisting systems or in robot navigation. However, frequently the image data is corrupted by noise and artifacts. In infrared thermography, temperature fluctuations due to reflections are often impossible to eliminate fully. In this paper, novel techniques will be presented which detect artifacts or problematic regions in image sequences. Optical flow computations based on local approaches such as those presented in Chap. 7 can then be enhanced by rejecting wrong estimates and inpainting the flow fields from neighboring areas. Furthermore, a joint Mumford Shah type approach for image restoration, image and motion edge detection and motion estimation from noisy image sequences is presented. This approach allows to restore missing information, which may be lost due to artifacts in the original image sequence. Finally, we discuss a Mumford Shah type model for motion estimation and restoration of frames from motion-blurred image sequences.

1.5.1 Modeling and Preprocessing

Standard Motion Model

The estimation of motion from image sequences represents a classical inverse problem. As such, constraint equations that relate motion to image intensities and changes thereof are required. In Chapt. 7, a wide range of these motion models is presented. Here we will just introduce the simplest one, keeping in mind that the proposed algorithms based upon this model can readily be extended to more complicated ones.

For a finite time interval $[0, T]$ and a spatial domain $\Omega \subset \mathbb{R}^d$ with $d = 1, 2, 3$ the image sequence $u : D \rightarrow \mathbb{R}$ is defined on the space time domain $D = [0, T] \times \Omega$. If $x : [0, T] \rightarrow \mathbb{R}^d$ describes the trajectory of a point of an object such that the velocity $w = (1, v)$ is given by $\dot{x} = w$ we can model a constant brightness intensity u as $u(t, x(t)) = \text{const}$. A first order approximation yields

$$\frac{du}{dt} = 0 \quad \Leftrightarrow \quad \frac{\partial u}{\partial t} + v \cdot \nabla_{(x)} u = 0 \quad \Leftrightarrow \quad w \cdot \nabla_{(t,x)} u = 0, \quad (1.15)$$

where ∇ is the gradient operator with respect to parameters given as indices. Models based on this equation called *differential models* since they are based on derivatives.

The parameters w of the motion model (1.15) can be solved by incorporating additional constraints such as local constancy of parameters or global smoothness (a more refined approach of assuming global piecewise smoothness will be presented in Sect. 1.5.2). Refined techniques for local estimates extending the common structure tensor approach have been outlined in Chapt. 7 and will not be repeated here.

Comparison of Confidence and Situation Measures and Their Optimality for Optical Flows

In order to detect artifacts in image sequences, one can analyze confidence and situation measures. Confidence measures are used to estimate the correctness of flow fields, based on information derived from the image sequence and/or the displacement field. Since no extensive analysis of proposed confidence measures has been carried out so far, in Kondermann et al. [2007a] we compare a comprehensive selection of previously proposed confidence measures based on the theory of intrinsic dimensions Zetzsche and Barth [1990], which have been applied to analyze optical flow methods in Kalkan et al. [2004]. We find that there are two kinds of confidence measures, which we distinguish into situation and confidence measures. Situation measures are used to detect locations, where the optical flow cannot be estimated unambiguously. This is contrasted by confidence measures, which are suited for evaluating the degree of accuracy of the flow field based. Situation measures can be applied, e.g., in image reconstruction Masnou and Morel [1998], to derive dense reliable flow

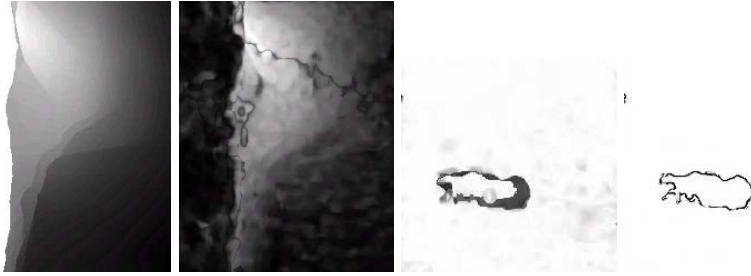


Fig. 1.7. Comparison of optimal confidence measure (left) to best known confidence measure (right) for Yosemite and Street sequences

fields Spies and Garbe [2002] or to choose the strength of the smoothness parameter in global methods (e.g., indirectly mentioned in Lai and Vemuri [1995]). Confidence measures are important for quantifying the accuracy of the estimated optical flow fields. A successful way to obtain robustness to noise in situation and confidence measures is also discussed in Kondermann et al. [2007a].

Previously, confidence measures employed were always chosen as innate to the flow estimation technique. By combining flow methods with non-inherent confidence measures we were able to show considerable improvements for confidence and situation measures. Altogether the results of the known measures are only partially satisfactory as many errors remain undetected and a large number of false positive error detections have been observed. Based on a derived optimal confidence map we obtain the results in Fig. 1.7 for Lynn Quam’s Yosemite sequence Heeger [1987], and the Street McCane et al. [2001] test sequences. For situation measures we conclude by presenting the best measure for each intrinsic dimension. Quantitative results can be found in Kondermann et al. [2007a].

An Adaptive Confidence Measure Based on Linear Subspace Projections

For variational methods, the inverse of the energy after optimization has been proposed as a general confidence measure in Bruhn and Weickert [2006]. For methods not relying on global smoothness assumptions, e.g. local methods, we propose a new confidence measure based on linear subspace projections in Kondermann et al. [2007b]. The idea is to derive a spatio-temporal model of typical flow field patches using e.g. principal component analysis (PCA). Using temporal information the resulting eigenflows can represent complex temporal phenomena such as a direction change, a moving motion discontinuity or a moving divergence. Then the reconstruction error of the flow vector is used to define a confidence measure.

Quantitative analysis shows that using the proposed measure we are able to improve the previously best results by up to 31%. A comparison between

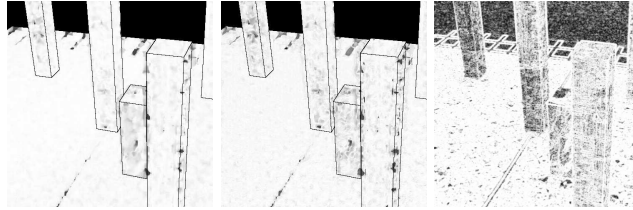


Fig. 1.8. Comparison to optimal confidence, left: optimal confidence map, center: pcaReconstruction confidence map, right: previously often used gradient confidence measure

the optimal, the obtained confidence and the previously often applied gradient measure Arredondo et al. [2004], Bruhn and Weickert [2006] is shown in Fig. 1.8.

Surface Situation Measures

In Kondermann et al. [2007c] we present a new type of situation measure for the detection of positions in the image sequence, where the full optical flow cannot be estimated reliably (e.g. in the case of occlusions, intensity changes, severe noise, transparent structures, aperture problems or homogeneous regions), that is in unoccluded situations of intrinsic dimension two. The idea is based on the concept of surface functions. A surface function for a given flow vector v reflects the variation of a confidence measure c over the set of variations of the current displacement vector.

$$S_{x,v,c} : \mathbb{R}^2 \rightarrow [0, 1], \quad S_{x,v,c}(d) := c(x, v + d). \quad (1.16)$$

By analyzing the curvature of a given surface function statements on the intrinsic dimension and possible occlusions can be made. The surface situation measures have proven superior to all previously proposed measures and are robust to noise as well.

1.5.2 Restoration of Optical Flows

Optical Flows via Flow Inpainting Using Surface Situation Measures

Based on the surface situation measures introduced in Sect. 1.5.1, in Kondermann et al. [2007c] we suggest a postprocessing technique for optical flow methods, a flow inpainting algorithm, which integrates the information provided by these measures and obtains significantly reduced angular errors. We demonstrate that 100% dense flow fields obtained from sparse fields via flow inpainting are superior to dense flow fields obtained by local and global methods. Table 1.1 shows the reduction of the angular error of four flow fields

Table 1.1. Original and inpainting angular error for surface measures and inpainting error based on the best previously known situation measure Kondermann et al. [2007a] on average for ten frames of the test sequences for the combined local global and the structure tensor method

	Combined Local Global		Structure Tensor	
	original	inpainting	original	inpainting
Marble	3.88 ± 3.39	3.87 ± 3.38	4.49 ± 6.49	3.40 ± 3.56
Yosemite	4.13 ± 3.36	3.85 ± 3.00	4.52 ± 10.10	2.76 ± 3.94
Street	8.01 ± 15.47	7.73 ± 16.23	5.97 ± 16.92	4.95 ± 13.23
Office	3.74 ± 3.93	3.59 ± 3.93	7.21 ± 11.82	4.48 ± 4.49

computed by a the local structure tensor (ST) Bigün et al. [1991] and the global combined local global (CLG) method Bruhn et al. [2005] by means of flow inpainting.

Comparing the angular error obtained by the derived flow inpainting algorithm to the angular error of the original flow fields computed with two state of the art methods (the fast local structure tensor method and the highly accurate combined local global method) we could achieve up to 38% lower angular errors and an improvement of the angular error in all cases. We conclude that both local and global methods can be used alike to obtain dense optical flow fields with lower angular errors than state of the art methods by means of the proposed flow inpainting algorithm. The algorithm was also used to compute accurate flow fields on real world applications. In Fig. 1.9 two examples for typical applications are presented. The inpainting algorithm significantly reduces errors due to reflections in thermographic image sequences of the air-water interface and errors in different situations in traffic scenes.

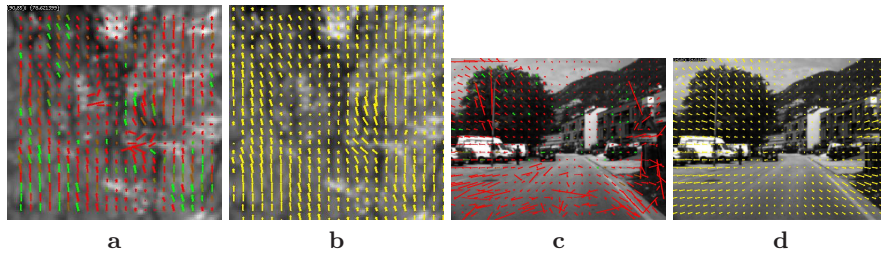


Fig. 1.9. In (a) the estimated flow field based on the structure tensor is shown for an infrared sequence of the air-water interface. Reflections lead to wrong estimates. The post processed motion field is shown in (b). In (c) and (d) the same is shown for a traffic scene.

Joint Estimation of Optical Flow, Segmentation and Denoising

In the previous section, separate techniques for detecting artifacts were presented, followed by an algorithm to inpaint parts of the flow field corrupted by the artifacts. In this section we will outline a technique for jointly denoising an image sequence, estimating optical flow and segmenting the objects at the same time Telea et al. [2006]. Our approach is based on an extension of the well known Mumford Shah functional which originally was proposed for the joint denoising and segmentation of still images. Given a noisy initial image sequence $u_0 : D \rightarrow \mathbb{R}$ we consider the energy

$$\begin{aligned} E_{\text{MSopt}}[u, w, S] &= \int_D \frac{\lambda_u}{2} (u - u_0)^2 \, d\mathcal{L} + \int_{D \setminus S} \frac{\lambda_w}{2} (w \cdot \nabla_{(t,x)} u)^2 \, d\mathcal{L} \\ &\quad + \int_{D \setminus S} \frac{\mu_u}{2} |\nabla_{(t,x)} u|^2 \, d\mathcal{L} \\ &\quad + \int_{D \setminus S} \frac{\mu_w}{2} |P_\delta[\zeta] \nabla_{(t,x)} w|^2 \, d\mathcal{L} + \nu \mathcal{H}^d(S) \end{aligned}$$

for a piecewise smooth denoised image sequence $u : D \rightarrow \mathbb{R}$, and a piecewise smooth motion field $w = (1, v)$ and a set $S \subset D$ of discontinuities of u and w . The first term models the fidelity of the denoised image-sequence u , the second term represents the fidelity of the flow field w in terms of the optical flow equation (1.15). The smoothness of u and w is required on $D \setminus S$ and finally, the last term is the Hausdorff measure of the set S . A suitable choice of the projection $P_\delta[\zeta]$ leads to an anisotropic smoothing of the flow field along the edges indicated by ζ .

The model is implemented using a phase field approximation in the spirit of Ambrosio and Tortorelli's approach Ambrosio and Tortorelli [1992]. Thereby the edge set S is replaced by a phase field function $\zeta : D \rightarrow \mathbb{R}$ such that $\zeta = 0$ on S and $\zeta \approx 1$ far from S . Taking into account the Euler-Lagrange equations of the corresponding yields a system of three partial differential equations for the image-sequence u , the optical flow field v and the phase field ζ :

$$\begin{aligned} -\operatorname{div}_{(t,x)} \left(\frac{\mu_u}{\lambda_u} (\zeta^2 + k_\epsilon) \nabla_{(t,x)} u + \frac{\lambda_w}{\lambda_u} w (\nabla_{(t,x)} u \cdot w) \right) + u &= u_0 \\ -\epsilon \Delta_{(t,x)} \zeta + \left(\frac{1}{4\epsilon} + \frac{\mu_u}{2\nu} |\nabla_{(t,x)} u|^2 \right) \zeta &= \frac{1}{4\epsilon} \\ -\frac{\mu_w}{\lambda_w} \operatorname{div}_{(t,x)} (P_\delta[\zeta] \nabla_{(t,x)} v) + (\nabla_{(t,x)} u \cdot v) \nabla_{(x)} u &= 0. \end{aligned} \tag{1.17}$$

For details on this approximation and its discretization we refer to Droske et al. [2007].

In Fig. 1.10 we show results from this model on a noisy test-sequence where one frame is completely missing. But this does not hamper the restoration of the correct optical flow field shown in the fourth column, because of the

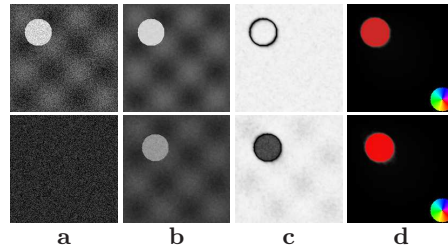


Fig. 1.10. Noisy test sequence: From top to bottom frames 9 and 10 are shown. (a) original image sequence, (b) smoothed images, (c) phase field, (d) estimated motion (color coded)



Fig. 1.11. Pedestrian video: frames from original sequence (left); phase field (middle); optical flow, color coded (right)

anisotropic smoothing of information from the surrounding frames into the destroyed frame.

Furthermore, in Fig. 1.11 we consider a complex, higher resolution video sequence showing a group of walking pedestrians. The human silhouettes are well extracted and captured by the phase field. The color-coded optical flow plot shows how the method is able to extract the moving limbs of the pedestrians.

Joint Motion Estimation and Restoration of Motion Blur

Considering video footage from a standard video camera, it is quite noticeable that relatively fast moving objects appear blurred. This effect is called *motion blur*, and it is linked to the aperture time of the camera, which roughly speaking integrates information in time. The actual motion estimation suffers from motion blur and on the other hand given the motion the blur can be removed by “deconvolution”. Hence, these two problems are intertwined, which motivates the development of a method that tackles both problems at once. In Bar et al. [2007] a corresponding joint motion estimation and deblurring model has been presented. For simplicity let us assume that an object is moving with constant velocity v in front of a still background and we observe m frames g_1, \dots, u_m at times t_1, \dots, t_m . From the object and background intensity functions f_{obj} and f_{bg} , respectively, one assembles the actual scene intensity func-



Fig. 1.12. From two real blurred frames (left), we automatically and simultaneously estimate the motion region, the motion vector, and the image intensity of the foreground (middle). Based on this and the background intensity we reconstruct the two frames (right)

tion $f(t, x) = f_{\text{obj}}(x - tv)\chi_{\text{obj}}(x - vt) + f_{\text{bg}}(x)(1 - \chi_{\text{obj}}(x - vt))$. Now, it turns out to be crucial close to motion edges to observe that the theoretically observed motion blur at time t is a properly chosen average of background intensity and motion blurred object intensity. Indeed, the expected intensity is given by $G_i[\Omega_{\text{obj}}, v, f_{\text{obj}}, f_{\text{bg}}](x) := ((f_{\text{obj}}\chi_{\text{obj}}) * h_v)(x - t_i v) + f_{\text{bg}}(x)(1 - (\chi_{\text{obj}} * h_v)(x - t_i v))$, where χ_{obj} is the characteristic function of the object domain Ω_{obj} and $h_v := \delta_0((v^\perp / |v|) \cdot y)h((v / |v|) \cdot y)$ a one dimensional filter kernel with filter width $\tau|v|$ in the direction of the motion trajectory $\{y = x + sv : s \in \mathbb{R}\}$. Here v^\perp denotes v rotated by 90 degrees, δ_0 is the usual 1D Dirac distribution and h the 1D block filter with $h(s) = 1 / (\tau|v|)$ for $s \in [-(\tau|v|) / 2, (\tau|v|) / 2]$ and $h(s) = 0$, else. Hence, a Mumford Shah type approach for joint motion estimation and deblurring comes along with the energy

$$E[\Omega_{\text{obj}}, v, f_{\text{obj}}] = \sum_{i=1,2} \int_{\Omega} (G_i[\Omega_{\text{obj}}, v, f_{\text{obj}}, f_{\text{bg}}] - g_i)^2 d\mathcal{L} + \int_{\Omega} \mu |\nabla f_{\text{obj}}| d\mathcal{L} + \nu |\partial \Omega_{\text{obj}}|$$

depending on the unknown object domain Ω_{obj} , unknown velocity v , object intensity f_{obj} to be restored. We ask for a minimizing set of the degrees of freedom Ω_{obj} , v , and f_{obj} . Once a minimizer is known, we can retrieve the deblurred images (see Fig. 1.12). For details on this approach and further results we refer to Bar et al. [2007].

1.6 FEM Techniques for Multiscale Visualization of Time-Dependent Flow Fields

The analysis and post-processing of flow fields is one of the fundamental tasks in scientific visualization. Sophisticated multiscale methods are needed to visualize and analyze the structure of especially nonstationary flow fields for which the standard tools may fail. A huge variety of techniques for the visualization of steady as well as time-dependent flow fields in 2D and 3D has been presented during the last years. The methods currently available range

from particle tracing approaches Turk and Banks [1996], van Wijk [1993] over texture based methods Diewald et al. [2000], van Wijk [1991], Cabral and Leedom [1993], Shen and Kao [1997], Interrante and Grosch [1997] to feature extraction for 3D flow fields Chong et al. [1990], Tobak and Peake [1982], Hunt et al. [1988], Jeong and Hussain [1995]. An overview is given by Laramée et al. [2004].

In this section we discuss the application of an anisotropic transport diffusion method to complex flow fields resulting from CFD computations on arbitrary grids. For general unstructured meshes, we apply the discretization of the arising transport diffusion problems by the streamline-diffusion (SD) FEM scheme, and we discuss iterative solvers of type Krylov-space or multi-grid schemes for the arising nonsymmetric auxiliary problems. We analyze a corresponding balancing of the involved operators and blending strategies. The application to several test examples shows that the approaches are excellent candidates for efficient visualization methods of highly nonstationary flow with complex multiscale behavior in space and time.

Moreover we show a technique for multiscale visualization of static flow fields which is based on an algebraic multigrid method. Starting from a standard finite element discretization of the anisotropic diffusion operator, the algebraic multigrid yields a hierarchy of inter-grid prolongation operators. These prolongations can be used to define coarse grid finite element basis functions whose support is aligned with the flow field.

1.6.1 The Anisotropic Transport Diffusion Method

In Bürkle et al. [2001], Preusser and Rumpf [2000] special methods which are based on anisotropic diffusion and transport anisotropic diffusion for the visualization of static and time-dependent vector fields have been presented. In this section we briefly review these models, the according parameters and a blending strategy which is needed to produce a visualization of time-dependent flow fields.

The Transport Diffusion Operator

We consider a time-dependent vector field $v : I \times \Omega \rightarrow \mathbb{R}^d$, $(s, x) \mapsto v(s, x)$ given on a finite time-space cylinder $I \times \Omega$ where $I = [0, T]$ and $\Omega \subset \mathbb{R}^d$ for $d = 2, 3$. Here, we restrict to $d = 2$. If the vector field v is constant in time, i.e., $v(s, x) = v_0(x)$ for all $s \in I$, we can create a multiscale visualization of the flow field in form of a family of textures $\{u(t)\}_{t \in \mathbb{R}^+}$ by the following anisotropic diffusion equation:

Find $u : \mathbb{R}^+ \times \Omega \rightarrow \mathbb{R}$ such that

$$\begin{aligned} \partial_t u - \operatorname{div}(A(v, \nabla u) \nabla u) &= f(u) && \text{in } \mathbb{R}^+ \times \Omega, \\ A(v, \nabla u) \partial_n u &= 0 && \text{on } \mathbb{R}^+ \times \partial\Omega, \\ u(0, \cdot) &= u_0(\cdot) && \text{in } \Omega. \end{aligned} \tag{1.18}$$

We start this evolution with an initial image u_0 showing random white noise. Since we have assumed the vector field to be continuous, there exists a family of orthogonal mappings $B(v) \in SO(d)$ such that $B(v)e_1 = v$. And denoting the identity matrix of dimension d with Id_d , the diffusion tensor reads

$$A(v, \nabla u) = B(v) \begin{pmatrix} \alpha(\|v\|) & 0 \\ 0 & G(\|\nabla u\|)\text{Id}_{d-1} \end{pmatrix} B(v)^T$$

where α is a monotone increasing function which prescribes a linear diffusion in direction of v for $\|v\| > 0$. We will choose α appropriately below. During the evolution, patterns are generated which are aligned with the flow field. The function $G(s) := \varepsilon/(1 + cs^2)$ – well known in image processing Perona and Malik [1987] – controls the diffusion in the directions orthogonal to the flow. It is modeled such that the evolution performs a clustering of streamlines and thus generates coarser representations of the vector field with increasing scale t . The definition of the diffusion tensor G depends on the gradient of a regularized image $u^\sigma = u * \chi^\sigma$. This regularization is theoretically important for the well-posedness of the presented approach Kawohl and Kutev [1998], Catté et al. [1992]. To our experience, in the implementation this regularization can be neglected or can be replaced by a lower bound for the value of $G(\cdot)$. For $\|v\| = 0$ we use an isotropic diffusion operator. The role of the right hand side $f(u)$ (1.18) is to strengthen the contrast of the image during the evolution, because for $f = 0$ the asymptotic limit would be an image of constant gray value. We set $f(u) = \rho \times ((2u - 1) - (2u - 1)^3)$ with $\rho = 80$ to increase the set of asymptotic states of the evolution. An example⁹ of the multiscale evolution is shown in Fig. 1.13, where the multiscale visualization of a flow field is displayed for the Venturi pipe problem in 2D Acker [to appear in 2008].

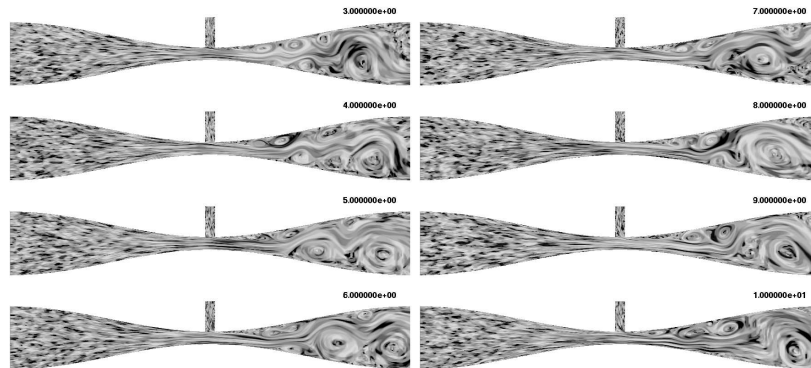


Fig. 1.13. Multiscale visualization of the Venturi Pipe example (with transport)

⁹ This example was computed with a time step of $\Delta t = 0.005$ on a mesh with 82753 nodes.

Let us now suppose that the vector field varies smoothly in time. If we would consider the evolution equation separately for each fixed time $s \in I$, the resulting textures at a fixed scale $t_0 \in \mathbb{R}^+$ would not give a smooth animation of the flow in time. This is due to a lack of correlation between the line-structures of the separate textures. However, if there would be a correlation between the structure of separate textures, the resulting animation would only give an Eulerian type representation of the flow.

To obtain a Lagrangian type representation, we consider the following anisotropic transport diffusion operator for the multiscale representation $u : \mathbb{R}^+ \times \Omega \rightarrow \mathbb{R}$ and the corresponding inhomogeneous transport diffusion equation

$$\begin{aligned} \partial_t u + v \cdot \nabla u - \operatorname{div}(A(v, \nabla u) \nabla u) &= f(u) && \text{in } \mathbb{R}^+ \times \Omega, \\ A(v) \partial_n u &= 0 && \text{on } \mathbb{R}^+ \times \partial\Omega, \\ u(0, \cdot) &= u_0(\cdot) && \text{in } \Omega. \end{aligned} \tag{1.19}$$

In this equation we have identified the time s of the vector field with the scale t of the multiscale visualization. Indeed the resulting texture shows again structures aligned with streamlines which are now transported with the flow. But due to the coupling of s and t the feature scale gets coarser with increasing time, i.e., we are not able to fix a scale t_0 and typically an animation is created at this scale showing always patterns of the same size. This fact makes the use of an appropriate blending strategy unavoidable.

Balancing the Parameters

In general the transport and the diffusion of the patterns of the texture u are opposite processes. Denoting a time-step of the transport diffusion equation with Δt and introducing the balance parameter $\beta > 0$ we have Bürkle et al. [2001]

$$\alpha(\|v\|)(x) = \frac{\beta^2 \max(\|v(x)\|, \|v\|_{min})^2 \Delta t}{2}.$$

In our applications we use the setting $\beta = 10$ and $\|v\|_{min} = 0.05$.

Blending Strategies

Blending strategies have to be used to get a visual representation of a given flow inside of a desired feature scale range. This means we have a set of solutions each started at a different time representing different feature scales which will be blended together. Different blending strategies are possible, e.g., trigonometric functions, interpolating splines, etc. We are currently using a Bézier-spline based approach combined with a specialized startup phase.

At the startup phase we will bootstrap our blending from one solution to the final number n_{tot} of solutions. The solutions are handled in an array. After

time Δt_{blend} , the oldest solution will be overwritten with noise and a ring shift will be carried out that brings the second oldest solution to the position of the oldest. In the startup phase a start solution containing noise is inserted at the start of the array and all other solutions are shifted one index position higher.

Is it obvious that the use of more blended solutions increases the smoothness of the transitions between visible feature scales. However, the computational time increases linearly with the number of used solutions which comes down to a tradeoff between quality and time. For preview purposes, two blended solutions are sufficient. High quality visualizations will need more.

1.6.2 Discretization

A Finite Element Discretization for Static Flow Fields

For static flow fields and the scheme (1.18) we can use a standard finite element method on a given discretizational grid of the domain. A semi-implicit Backward Euler scheme with time step width Δt is applied, which results in the evaluation of the diffusion tensor A and the right hand side f at the previous time steps. This leads to the semi-discrete scheme

$$\frac{u_{n+1} - u_n}{\Delta t} - \operatorname{div}(A(v_{n+1}, \nabla u_n) \nabla u_{n+1}) = f(u_n), \quad (1.20)$$

where u_n denotes the evaluation of u at time $n\Delta t$. Denoting the finite element basis functions with ϕ_i the spatial discretization yields the well known mass matrix M with entries $M_{ij} = \int_{\Omega} \phi_i \phi_j dx$ and the stiffness matrix L^n at time step n with entries $L_{ij}^n = \int_{\Omega} A(v_n) \nabla \phi_i \cdot \nabla \phi_j$. In summary we get a system of equations $(M + (\Delta t)L^{n-1})U^n = MU^{n-1} + F^{n-1}$ for the vector U^n of nodal values of u^n . This system can be solved with e.g. a conjugate gradient method.

The SD Finite Element Method for Time-Dependent Flow Fields

In Bürkle et al. [2001] a characteristic-upwinding algorithm due to Pironneau Pironneau [1982] is used to discretize the transport diffusion scheme (1.19) on quadtree/octtree grids for $\Omega = [0, 1]^d$. For the diffusive parts and the right hand side again a semi-implicit Backward Euler scheme with time-step Δt is applied (cf. (1.20)):

$$\frac{u_{n+1} - u_n}{\Delta t} + v_{n+1} \cdot \nabla u_{n+1} - \operatorname{div}(A(v_{n+1}, \nabla u_n) \nabla u_{n+1}) = f(u_n). \quad (1.21)$$

However the application of the anisotropic diffusion visualization method on rectangular or cubical domains is often unrealistic in complex CFD applications. Moreover, vector field data typically coming from CFD simulations is rarely given on structured quadtree/octtree grids. Furthermore, the scheme

introduces some numerical diffusion which decreases the quality of the final animation. In this section we discuss a higher order discretization scheme on general meshes which leads to high quality animations, showing sharp patterns moving with the flow field.

The variational formulation of (1.21) reads

$$\begin{aligned} (u_{n+1}, \psi) + \Delta t (v_{n+1} \cdot \nabla u_{n+1}, \psi) + \Delta t (A(v_{n+1}, \nabla u_n) \nabla u_{n+1}, \nabla \psi) &= (1.22) \\ \Delta t (f(u_n), \psi) + (u_n, \psi) \quad \forall \psi \in \mathcal{V} &(1.23) \end{aligned}$$

with the space of test-functions \mathcal{V} and test functions $\psi \in \mathcal{V}$.

The convection part of our equation demands some kind of additional stabilization. Since the diffusion operator A is already decomposed, in a way that allows to control the diffusion in flow direction, we replace A with a slightly modified version \tilde{A} :

$$\tilde{A}(v, \nabla u) = B(v) \begin{pmatrix} \alpha(\|v\|) + sd & 0 \\ 0 & G(\|\nabla u\|) \text{Id}_{d-1} \end{pmatrix} B(v)^T.$$

This modification allows an easy implementation of the streamline-diffusion scheme. The scalar function sd is the necessary *streamline diffusion* added in flow direction and is computed by

$$Re_{loc} := \frac{\|v\|_{loc} h_{loc}}{\alpha(\|v\|)}, \quad sd := sd_{par} h_{loc} \frac{Re_{loc}}{1 + Re_{loc}}.$$

The parameter $sd_{par} \in (0, 2)$, is user-specified and h_{loc} is the local mesh width, that means defined on each mesh cell, analogously to $\|v\|_{loc}$ as local flow speed (see Turek [1999] for more details). The advantage of this scheme is that it can be easily applied on general unstructured meshes, giving sufficient robustness for treating the convection dominated parts while at the same time the amount of numerical diffusion is not too big. Moreover, since it is a *linear scheme* - in contrast to TVD methods - the resulting subproblems are linear and can be efficiently treated via standard iterative solvers. However, being a linear scheme, the SD scheme suffers potentially from spurious numerical oscillations, due to over and undershooting, and the choice for the user-specific parameter sd_{par} can be critical. In a forthcoming paper, we plan to analyze the influence of the parameter sd_{par} onto the behavior of accuracy, robustness and efficiency of the described numerical approaches.

1.6.3 Multiscale Analysis with Algebraic Multigrid (AMG)

In Griebel et al. [2004] we use the fact that the structure of the flow is completely encoded in the diffusion operator $-\text{div}(A(v, \nabla u) \nabla u)$ to create a multiscale representation of the flow field. Let us assume that we have discretized the diffusion operator by standard finite elements on a regular grid yielding the stiffness-matrix L introduced in Subsect. 1.6.2. The algebraic multigrid

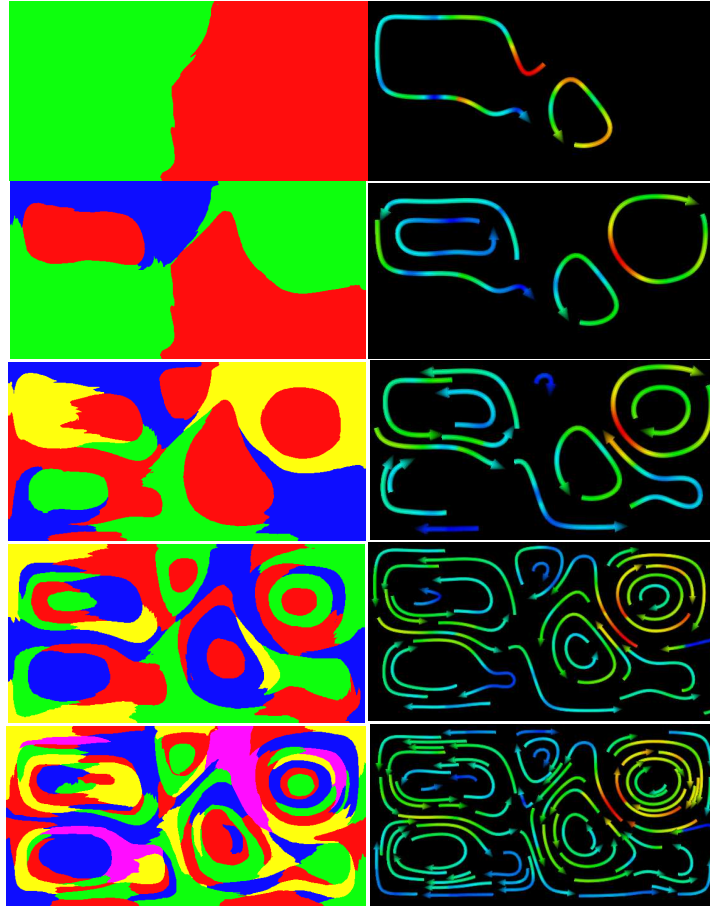


Fig. 1.14. Multiscale visualization of a convective flow using AMG. The left column shows flow field clusters which are obtained from the supports of basis functions at different grid levels. The right column shows a representation of the clusters with arrow icons. The grid level increases from top to bottom

method (AMG) finds a hierarchy of finite element basis functions which leads to optimal convergence of a multigrid solver of the linear system of equations determined by L . Thereby it generates a set of inter-grid prolongation matrices P^k which define the coarse grid basis.

Since the structure of the flow is encoded into the discretized diffusion operator, the AMG aligns the support of coarse grid basis functions to the diffusion of mass along the vector field. Consequently the prolongation matrices can be used for a multiscale visualization of flow fields. In Fig. 1.14 we show the AMG multiscale representation of the vector field of a convective flow.

1.6.4 Conclusions and Outlook

We have discussed multiscale visualization techniques for time-dependent and static flow fields coming from CFD simulations on general 2D and 3D domains. The proposed models are based on PDEs with anisotropic transport and diffusion operators which are linearized in time by a semi-implicit approach. The simple diffusion problem can be discretized by a standard FEM scheme, for the transport diffusion scheme the resulting problem in each time step is discretized by a sophisticated streamline-diffusion FEM scheme on unstructured quadrilateral grids. The main features of the proposed numerical methods together with improved blending strategies and a discussion of the involved parameters have been tested via numerical examples.

In a next step, the use of the Crank-Nicholson or a related 2nd order time stepping scheme, for instance fractional-step- θ -methods (see Turek et al. [2005]), will be analyzed which we expect to yield better accuracy results and hence enables for the use of larger time steps. Another aspect is the improvement of the iterative solvers, particularly of special multigrid schemes which are able to cope with the very anisotropic differential operators and the related very ill-conditioned linear systems. These fast solvers and improved variants of the streamline-diffusion or monotone and oscillation-free FEM-TVD techniques (cf. Kuzmin and Turek [2004]) will be the key ingredients for efficient visualization tools for complex 3D flows.

References

- J.F. Acker. *PDE basierte Visualisierungsmethoden für instationäre Strömungen auf unstrukturierten Gittern*. PhD thesis, Universität Dortmund, to appear in 2008.
- L. Ambrosio and V. M. Tortorelli. On the approximation of free discontinuity problems. *Boll. Un. Mat. Ital. B*, 6(7):105–123, 1992.
- L. Ambrosio, N. Fusco, and D. Pallara. *Functions of bounded variation and free discontinuity problems*. Oxford Mathematical Monographs. The Clarendon Press, New York, 2000.
- M. Arredondo, K. Lebart, and D. Lane. Optical flow using textures. *Pattern Recognition Letters*, 25(4):449–457, 2004.
- R. Bajcsy and C Broit. Matching of deformed images. In *Proc. 6th Int. Joint Conf. Patt Recogn.*, pages 351–353, 1982.
- J.M. Ball. Global invertibility of sobolev functions and the interpenetration of matter. *Proceedings of the royal Society of Edinburgh*, 88A:315–328, 1981.
- L. Bar, B. Berkels, M. Rumpf, and G. Sapiro. A variational framework for simultaneous motion estimation and restoration of motion-blurred video. In *Proceedings ICCV*, to appear, 2007.
- J. Bigün, G.H. Granlund, and J. Wiklund. Multidimensional orientation estimation with applications to texture analysis and optical flow. *IEEE PAMI*, 13(8):775–790, 1991.

- V. Blanz and T. Vetter. A morphable model for the synthesis of 3d faces. In *Proceedings of SIGGRAPH 99*, Computer Graphics Proceedings, Annual Conference Series, pages 187–194, 1999.
- K. Bredies. *Optimal control of degenerate parabolic equations in image processing*. PhD thesis, University of Bremen, 2007.
- K. Bredies, D. A. Lorenz, and P. Maass. A generalized conditional gradient method and its connection to an iterative shrinkage method. To appear in *Comput. Optim. Appl.*, 2008.
- L. Gottesfeld Brown. A survey of image registration techniques. *ACM Computing Surveys*, 24(4):325–376, 1992.
- A. Bruhn and J. Weickert. A confidence measure for variational optic flow methods. In *Geometric Properties for Incomplete data*, pages 283–298. Springer-Verlag, 2006.
- A. Bruhn, J. Weickert, and C. Schnörr. Lucas/kanade meets horn/schunck: Combining local and global optic flow methods. *International Journal of Computer Vision*, 61(3):211–231, 2005.
- D. Bürkle, T. Preusser, and M. Rumpf. Transport and anisotropic diffusion in time-dependent flow visualization. In *Proceedings Visualization '01*, 2001.
- B. Cabral and L. Leedom. Imaging vector fields using line integral convolution. In James T. Kajiya, editor, *Computer Graphics (SIGGRAPH '93 Proceedings)*, volume 27, pages 263–272, August 1993.
- J. Capon. High-resolution frequency-wavenumber spectrum analysis. *Proceedings of the IEEE*, 57(8):1408–1418, 1969.
- F. Catté, P.-L. Lions, J.-M. Morel, and T. Coll. Image selective smoothing and edge detection by nonlinear diffusion. *SIAM J. Numer. Anal.*, 29(1):182–193, 1992.
- M. S. Chong, A.E. Perry, and B. J. Cantwell. A general classification of three-dimensional flow fields. *Phys. Fluids A*, 2(5):765–777, 1990.
- P. G. Ciarlet. *Three-Dimensional Elasticity*. Elsevier, New York, 1988.
- U. Clarenz, N. Litke, and M. Rumpf. Axioms and variational problems in surface parameterization. *Computer Aided Geometric Design*, 21 (8):727 – 749, 2004.
- U. Clarenz, M. Droske, S. Henn, M. Rumpf, and K. Witsch. Computational methods for nonlinear image registration. In O. Scherzer, editor, *Mathematical Method for Registration and Applications to Medical Imaging, Mathematics in Industry*, volume 10, 2006.
- A. Collignon and et al. Automated multi-modality image registration based on information theory. In Y. Bizais, editor, *Proc. Conf. Information Processing in Medical Imaging*, pages pp. 263–274, 1995.
- M. S. Diallo, M. Kulesh, M. Holschneider, and F. Scherbaum. Instantaneous polarization attributes in the time-frequency domain and wavefield separation. *Geophysical Prospecting*, 53(5):723–731, 2005.
- M. S. Diallo, M. Kulesh, M. Holschneider, K. Kurennaya, and F. Scherbaum. Instantaneous polarization attributes based on an adaptive approximate covariance method. *Geophysics*, 71(5):V99–V104, 2006a.

- M. S. Diallo, M. Kulesh, M. Holschneider, F. Scherbaum, and F. Adler. Characterization of polarization attributes of seismic waves using continuous wavelet transforms. *Geophysics*, 71(3):V67–V77, 2006b.
- U. Diewald, T. Preusser, and M. Rumpf. Anisotropic diffusion in vector field visualization on euclidean domains and surfaces. *Trans. Vis. and Comp. Graphics*, 6(2):139–149, 2000.
- M. Droske and W. Ring. A Mumford-Shah level-set approach for geometric image registration. *SIAM Appl. Math.*, 2007. to appear.
- M. Droske and M. Rumpf. A variational approach to non-rigid morphological registration. *SIAM Appl. Math.*, 64(2):668–687, 2004.
- M. Droske and M. Rumpf. Multi scale joint segmentation and registration of image morphology. *IEEE Transaction on Pattern Recognition and Machine Intelligence*, 2005. to appear.
- M. Droske, C. Garbe, T. Preusser, M. Rumpf, and A. Telea. A phase field method for joint denoising, edge detection and motion estimation. *SIAM Appl. Math.*, revised version submitted, 2007.
- L. Florack and A. Kuijper. The topological structure of scale-space images. *J. Math. Imaging Vis.*, 12(1):65–79, 2000. ISSN 0924-9907.
- U. Grenander and M. I. Miller. Computational anatomy: An emerging discipline. *Quarterly Appl. Math.*, 56(4):617–694, 1998.
- M. Griebel, T. Preusser, M. Rumpf, M.A. Schweitzer, and A. Telea. Flow field clustering via algebraic multigrid. In *Proceedings IEEE Visualization*, pages 35–42, 2004.
- X. Gu and B. C. Vemuri. Matching 3D shapes using 2D conformal representations. In *MICCAI 2004*, LNCS 3216, pages 771–780, 2004.
- D. Heeger. Model for the extraction of image flow. *Journal of the Optical Society of America*, 4(8):1455–1471, 1987.
- M. Holschneider. *Wavelets: an Analysis Tool*. Oxford: Clarendon Press, 1995.
- M. Holschneider, M. S. Diallo, M. Kulesh, M. Ohrnberger, E. Lück, and F. Scherbaum. Characterization of dispersive surface waves using continuous wavelet transforms. *Geophysical Journal International*, 163(2):463–478, 2005.
- J. C. R. Hunt, A. A. Wray, and P. Moin. Eddies, stream and convergence zones in turbulent flow fields. Technical Report CTR-S88, Center for turbulence research, 1988.
- V. Interrante and C. Grosch. Strategies for effectively visualizing 3D flow with volume LIC. In *Proceedings Visualization '97*, pages 285–292, 1997.
- J. Jeong and F. Hussain. On the identification of a vortex. *Journal of Fluid Mechanics*, 285:69–94, 1995.
- S. Kalkan, D. Calow, M. Felsberg, F. Worgotter, M. Lappe, and N. Kruger. Optic flow statistics and intrinsic dimensionality, 2004.
- E. R. Kanasevich. *Time Sequence Analysis in Geophysics*. University of Alberta Press, Edmonton, Alberta, 1981.
- B. Kawohl and N. Kutev. Maximum and comparison principle for one-dimensional anisotropic diffusion. *Math. Ann.*, 311 (1):107–123, 1998.

- C. Kondermann, D. Kondermann, B. Jähne, and C. Garbe. Comparison of confidence and situation measures and their optimality for optical flows. *submitted to International Journal of Computer Vision*, Feb. 2007a.
- C. Kondermann, D. Kondermann, B. Jähne, and C. Garbe. An adaptive confidence measure for optical flows based on linear subspace projections. In *Proc. of the DAGM*, 2007b. in press.
- C. Kondermann, D. Kondermann, B. Jähne, and C. Garbe. Optical flow estimation via flow inpainting using surface situation measures. *submitted*, 2007c.
- A. Kufner. *Weighted sobolev spaces*, 1980. Teubner-Texte zur Mathematik, volume 31.
- M. Kulesh, M. Holschneider, M. S. Diallo, Q. Xie, and F. Scherbaum. Modeling of wave dispersion using continuous wavelet transforms. *Pure and Applied Geophysics*, 162(5):843–855, 2005a.
- M. Kulesh, M. S. Diallo, M. Holschneider, K. Kurennaya, F. Krüger, M. Ohrnberger, and F. Scherbaum. Polarization analysis in the wavelet domain based on the adaptive covariance method. *Geophysical Journal International*, 2007a. in press.
- M. Kulesh, M. Holschneider, M. Ohrnberger, and E. Lüeck. Modeling of wave dispersion using continuous wavelet transforms II: wavelet based frequency-velocity analysis. Technical Report 154, Preprint series of the DFG priority program 1114 “Mathematical methods for time series analysis and digital image processing”, January 2007b.
- M. A. Kulesh, M. S. Diallo, and M. Holschneider. Wavelet analysis of ellipticity, dispersion, and dissipation properties of Rayleigh waves. *Acoustical Physics*, 51(4):421–434, 2005b.
- D. Kuzmin and S. Turek. High-Resolution FEM-TVD Schemes Based on a Fully Multidimensional Flux Limiter. *J. Comput. Phys.*, 198:131–158, 2004.
- S.H. Lai and B.C. Vemuri. Robust and efficient algorithms for optical flow computation. In *Proc. of Int. Symp. Comp. Vis.*, pages 455–460, November 1995.
- R.S. Laramée, H. Hausser, H. Doleisch, B. Vrolijk, F.H. Post, and D. Weiskopf. The state of the art in flow visualization: Dense and texture-based techniques. *Computer Graphics forum*, 23(2):203–221, 2004.
- A. Lee, D. Dobkin, W. Sweldens, and P. Schröder. Multiresolution mesh morphing. In *Proceedings of SIGGRAPH 99*, Computer Graphics Proceedings, Annual Conference Series, pages 343–350, August 1999.
- N. Litke, M. Droske, M. Rumpf, and P. Schröder. An image processing approach to surface matching. In M. Desbrun and H. Pottmann, editors, *Third Eurographics Symposium on Geometry Processing*, pages 207–216, 2005.
- S. Masnou and J. Morel. Level lines based disocclusion. In *Proc. of ICIP*, volume 3, pages 259 – 263, 1998.
- B. McCane, K. Novins, D. Crannitch, and B. Galvin. On benchmarking optical flow. <http://of-eval.sourceforge.net/>, 2001.

- M.I. Miller, A. Trouvé, and L. Younes. On the metrics and euler-lagrange equations of computational anatomy. *Annual Review of Biomedical Engineering*, 4:375–405, 2002.
- I. B. Morozov and S. B. Smithson. Instantaneous polarization attributes and directional filtering. *Geophysics*, 61(3):872–881, 1996.
- O. A. Oleĭnik and E. V. Radkevič. Second order equations with nonnegative characteristic form. American Mathematical Society, 1973.
- F. Pacor, D. Bindi, L. Luzi, S. Parolai, S. Marzorati, and G. Monachesi. Characteristics of strong ground motion data recorded in the Gubbio sedimentary basin (Central Italy). *Bulletin of Earthquake Engineering*, 5(1): 27–43, 2007.
- H. A. Pedersen, J. I. Mars, and P.-O. Amblard. Improving surface-wave group velocity measurements by energy reassignment. *Geophysics*, 68(2):677–684, 2003.
- P. Perona and J. Malik. Scale space and edge detection using anisotropic diffusion. In *IEEE Computer Society Workshop on Computer Vision*, 1987.
- P. Perona and J. Malik. Scale-space and edge detection using anisotropic diffusion. Technical Report UCB/CSD-88-483, EECS Department, University of California, Berkeley, Dec 1988.
- C. R. Pinnegar. Polarization analysis and polarization filtering of three-component signals with the time-frequency S transform. *Geophysical Journal International*, 165(2):596–606, 2006.
- O. Pironneau. On the transport-diffusion algorithm and its applications to the Navier-Stokes equations. *Numer. Math.*, 38:309–332, 1982.
- W. H. Press, S. A. Teukolsky, W. T. Vetterling, and B. P. Flannery. *Numerical Recipe in C: The Art of Scientific Computing*. Cambridge University Press, 1992.
- T. Preusser and M. Rumpf. An adaptive finite element method for large scale image processing. *Journal of Visual Comm. and Image Repres.*, 11:183–195, 2000.
- M. Schimmel and J. Gallart. The inverse S-transform in filters with time-frequency localization. *IEEE Transaction on Signal Processing*, 53(11): 4417–4422, 2005.
- H.-W. Shen and D. L. Kao. Uflic: A line integral convolution algorithm for visualizing unsteady flows. In *Proceedings Visualization '97*, pages 317–322, 1997.
- N. Soma, H. Niitsuma, and R. Baria. Reflection technique in time-frequency domain using multicomponent acoustic emission signals and application to geothermal reservoirs. *Geophysics*, 67(3):928–938, 2002.
- H. Spies and C. Garbe. Dense parameter fields from total least squares. In L. Van Gool, editor, *Pattern Recognition*, volume LNCS 2449 of *Lecture Notes in Computer Science*, pages 379–386, Zurich, CH, 2002. Springer-Verlag.

- A. Telea, T. Preusser, C. Garbe, M. Droske, and M. Rumpf. A variational approach to joint denoising, edge detection and motion estimation. In *Proc. DAGM 2006*, pages 525–353, 2006.
- M. Tobak and D. J. Peake. Topology of 3D separated flow. *Ann. Rev. Fluid Mech.*, 14:61–85, 1982.
- S. Turek. *Efficient Solvers for Incompressible Flow Problems: An Algorithmic and Computational Approach*, volume 6 of *LNCSE*. Springer, 1999.
- S. Turek, L. Rivkind, J. Hron, and R. Glowinski. Numerical analysis of a new time-stepping θ -scheme for incompressible flow simulations, 2005. To appear in JSC.
- G. Turk and D. Banks. Image-guided streamline placement. In *Proc. 23rd annual conference on Computer graphics, August 4 - 9, 1996, New Orleans, LA USA*. ACM Press, 1996.
- J. J. van Wijk. Spot noise-texture synthesis for data visualization. In T. W. Sederberg, editor, *Computer Graphics (SIGGRAPH '91 Proceedings)*, volume 25, pages 309–318, July 1991.
- J. J. van Wijk. Flow visualization with surface particles. *IEEE Computer Graphics and Applications*, 13(4):18–24, July 1993.
- P. Viola and W.M. Wells. Alignment by maximization of mutual information. *International Journal of Computer Vision*, 24(2):137–154, 1997.
- J. Weickert. *Anisotropic Diffusion in Image Processing*. European Consortium for Mathematics in Industry. Teubner, Stuttgart, Leipzig, 1998.
- A. P. Witkin. Scale-space filtering. In *Proc. of the 8th IJCAI*, pages 1019–1022, Karlsruhe, Germany, 1983.
- Q. Xie, M. Holschneider, and M. Kulesh. Some remarks on linear diffeomorphisms in wavelet space. Technical Report 37, Preprint series of the DFG priority program 1114 "Mathematical methods for time series analysis and digital image processing", July 2003.
- C. Zetsche and E. Barth. Fundamental limits of linear filters in the visual processing of two dimensional signals. *Vision Research*, 30(7):1111–1117, 1990.

Index

- algebraic multigrid method, 35
- analysis
 - Fourier, 3
 - principal components, 5, 24
 - time-frequency, 3
- anisotropic diffusion, 30
- approximation
 - phase field, 27
- confidence measure, 23
- control
 - optimal, 16
- covariance method, 5
- degenerate diffusion, 18
- diffusion
 - anisotropic, 30
 - degenerate, 18
 - streamline, 34
 - transport, 30
- dispersion
 - wave, 6
- elasticity
 - nonlinear, 9
- equations
 - parabolic, 16
- finite element method, 33
- Fourier analysis, 3
- geometry images, 14
- heterogeneous media, 6
- image
 - mammography, 22
- image registration, 9
- images
 - geometry, 14
- inpainting, 25
- mammography image, 22
- measure
 - confidence, 23
 - situation, 23
- method
 - algebraic multigrid, 35
 - finite element, 33
- morphology, 9
- motion blur, 28, 29
- Mumford Shah, 11, 22
- nonlinear elasticity, 9
- optimal control, 16
- parabolic equations, 16
- phase field approximation, 27
- principal components analysis, 5, 24
- registration
 - image, 9
- situation measure, 23
- Sobolev spaces
 - weighted and directional, 20
- streamline diffusion, 34
- time-frequency analysis, 3
- transport diffusion, 30
- wave dispersion, 6
- wavelet transform, 3